Summer 2021

Transport Properties of Binary and Doped Diborides

Alin Babu Niraula
Missouri State University, Alin8@live.missouristate.edu

TRANSPORT PROPERTIES OF BINARY AND DOPED DIBORIDES

A Master's Thesis

Presented to

The Graduate College of

Missouri State University

In Partial Fulfillment

Of the Requirements for the Degree

Master of Science, Materials Science

By

Alin Babu Niraula

July 2021

TRANSPORT PROPERTIES OF BINARY AND DOPED DIBORIDES

Physics, Astronomy and Materials Science

Missouri State University, July 2021

Master of Science

Alin B Niraula

ABSTRACT

A systematic computational study to evaluate the electronic structures and transport properties including resistivity, thermal conductivity of several binary diborides (ZrB_2, TiB_2, TaB_2, CrB_2, and AlB_2) and the ZrB_2 alloyed with Cr, Al, Ti and Ta has been performed. Due to the p-d hybridization, the characteristic pseudo gap at the Fermi energy level (Ef) from the density of states (DOS) is presence in the DOS of both ZrB_2 and TiB_2 in contrast to those of TaB_2 and CrB_2 with only a partial occupation on the anti-bonding states. AlB_2 is also similarly shown the presence of pseudo gap in its DOS due to the degeneracy of p-bands from Al and B. These characteristic features in electronic structures in turns delineate the thermal conductivity behavior of the diborides and alloyed ZrB_2. I further showed, via the transport property calculations, that a simple additive rule could not necessarily be applied to predict the thermal conductivity of alloyed ZrB_2.

KEYWORDS: Transport Properties, diborides, doped ZrB_2, Thermal properties, DFT, EPW, Resistivity.

TRANSPORT PROPERTIES OF BINARY AND DOPED DIBORIDES

By

Alin Babu Niraula

A Master's Thesis
Submitted to the Graduate College
Of Missouri State University
In Partial Fulfillment of the Requirements
For the Degree of Master of Science, Materials Science

July 2021

Approved:

Ridwan Sakidja, Ph.D, Thesis Committee Chair

Kartik C. Ghosh, Ph.D, Committee Member

Tiglet Besara, Ph.D, Committee Member

Julie Masterson, Ph.D., Dean of the Graduate College

ACKNOWLEDGEMENTS

First and foremost, I am thankful to Dr. Ridwan Sakidja, my adviser, for allowing me to participate in this interesting research. These two years have been a wonderful learning curve full of obstacles, and his continual encouragement, wisdom, and inspiration have been helpful along the trip. This endeavor would not have been feasible without his passion and ideas. I would want to use this opportunity to express my gratitude to all the other faculty members, employees, and colleagues who have supported me throughout my tenure at Missouri State.

The financial support from CMMI Division of NSF (Award No. 1902069) is gratefully acknowledged. The computational allocation for the Cori supercomputers at NERSC in Lawrence Berkeley National Laboratory is also acknowledged.

Finally, I owe a debt of gratitude to my parents, Tulasi Prasad Niraula and Tara Niraula, for their unending sacrifices and willingness to share their goals and aspirations with me.

TABLE OF CONTENTS

LIST OF TABLES

LIST OF FIGURES

INTRODUCTION

Reusable atmospheric reentry vehicles for easier access to space, faster delivery of persons and goods, as well as aircraft and missile systems for combat uses such as rapid reaction strike missiles, have both sparked interest in the next generation hypersonic vehicle [1–4]. Sharp leading and trailing edges are recommended for future hypersonic vehicles to improve versatility. The temperatures produced at sharp leading edges, on the other hand, increase as the radius decreases and can reach over 2000 °C. Sharp leading edges are exposed to high heat fluxes produced by convective flow at the stagnation stage, in addition to high temperatures [1]. Rising thermal conductivity will improve heat transfer from the hot edge to the cooler areas where it is dissipated. As a result, improved thermal conductivity reduces thermal stresses and enhances thermal shock resistance in hypersonic aircraft, resulting in increased reliability and operating speeds [1]. As a result, cutting-edge materials for next-generation hypersonic vehicles should melt at temperatures above 2000°C and have strong fracture capabilities and thermal conductivities.

For high-temperature applications like reentry spacecraft, hypersonic vehicles, only the materials which can withstand extreme temperature (around 2000K) are applicable. Ultra-high temperature ceramics (UHTCs) like ZrB_2, HfB_2, TiB_2, TaB_2, etc have been explored for high-temperature application owing to their high melting point, high electrical and thermal conductivity, and high strength [5–8]. These ceramics can be of particularly skillful use to manage thermal diffusivity under the extreme thermal environment such as hyper-sonic vehicles and reentry spacecraft due to their high thermal conductivities [7]. Furthermore, in high heat flux situations, the high thermal conductivity increases thermal shock resistances [7].

The metal diborides like ZrB_2, TiB_2, TaB_2, CrB_2, and AlB_2 have hexagonal crystal structures with p6/mmm symmetry [9]. In this structure, the metal atoms are situated directly below/above six members rings of boron atoms.

While there have been many theoretical studies carried out in the past to understand the electronic structures and lattice properties of these ceramics within the framework of Density Functional Theory (DFT) approximation [10], none has been focused, particularly on the thermal conductivities.

The purpose of this research is to explore the basic transport properties of metal diborides and to provide a better understanding of the influence of dopants (Ti, Cr, Ta) on the thermal conductivity of ZrB_2.

LITERATURE REVIEW

Crystal Structures

The chemical, physical, and thermal properties of materials are determined by crystal chemistry and crystal structure. Borides come in a variety of formulations, with B: M ratios varying from 1:4 to 12:1. Both properties and electronic structure are controlled by the B: M ratio [2]. Altering the B: M ratio alters the boron's electronic structure, resulting in the creation of various structural complexes with one-, two-, and three-dimensional (3D) B networks [2]. Metal diborides like ZrB_2, TiB_2, TaB_2, CrB_2, and AlB_2 exhibit hexagonal crystal structure with p6/mmm space symmetry [9] as shown in Figure 1, with one transition metal atom and two boron atoms per unit cell. This crystal structure consists of B-B covalent bonds, M-M bonds, and M-B bonds in which B-B bonds contribute to its hardness and stability where M-B contributes to its high melting temperature [11]. B atoms are electron acceptors of diborides, while M atoms are electron donors. Each M atom donates two electrons (one to each B), transforming M into a doubly charged cation and B atoms into singly charged anions [2]. The first, second, and third closest neighbors for zirconium are 2.547 Å (out of Zr plane), 3.173 Å (in the Zr plane), and 4.069 Å (out of Zr plane) respectively [1]. Similarly, boron's first, second, and third closest neighbors are 1.832 Å (in the B plane), 2.547 Å (out of the B plane), and 3.664 Å (in the B plane) respectively [1]. Similarly, in the zirconium layer, the transition metal (TM) zirconium is precisely above the midpoint of the hexagonal boron ring in the boron layer. The zirconium atom is located at (0,0,0) in a unit cell, while two boron atoms are situated at (1/3, 2/3, 1/2) and (2/3, 1/3, 1/2). Other transition metals (TM) such as Hf, Ti, Va, and Nb may be substituted for zirconium and still hold the same structure (P6/mmm) as zirconium diboride. The lattice

parameter, on the other hand, is adjusted in line with the size of the transition metal that is being substituted by a zirconium atom. Because of the TM-TM and TM-B interactions, replacing zirconium atoms with transition metals would increase lattice parameters. TM-TM interaction characterizes the difference in lattice parameter along XY plane, while TM-B interaction characterizes the variation of lattice parameter along z-direction [1]. The differences in lattice constants a and c in modifying transition metal are unlikely due to TM-TM interaction along the plane and TM-B interaction out of the plane, with c normally increasing or decreasing more than lattice parameter a. Zr-Zr, Zr-B, and B-B contact, or bond power are all linked to structural stability in ZrB_2.

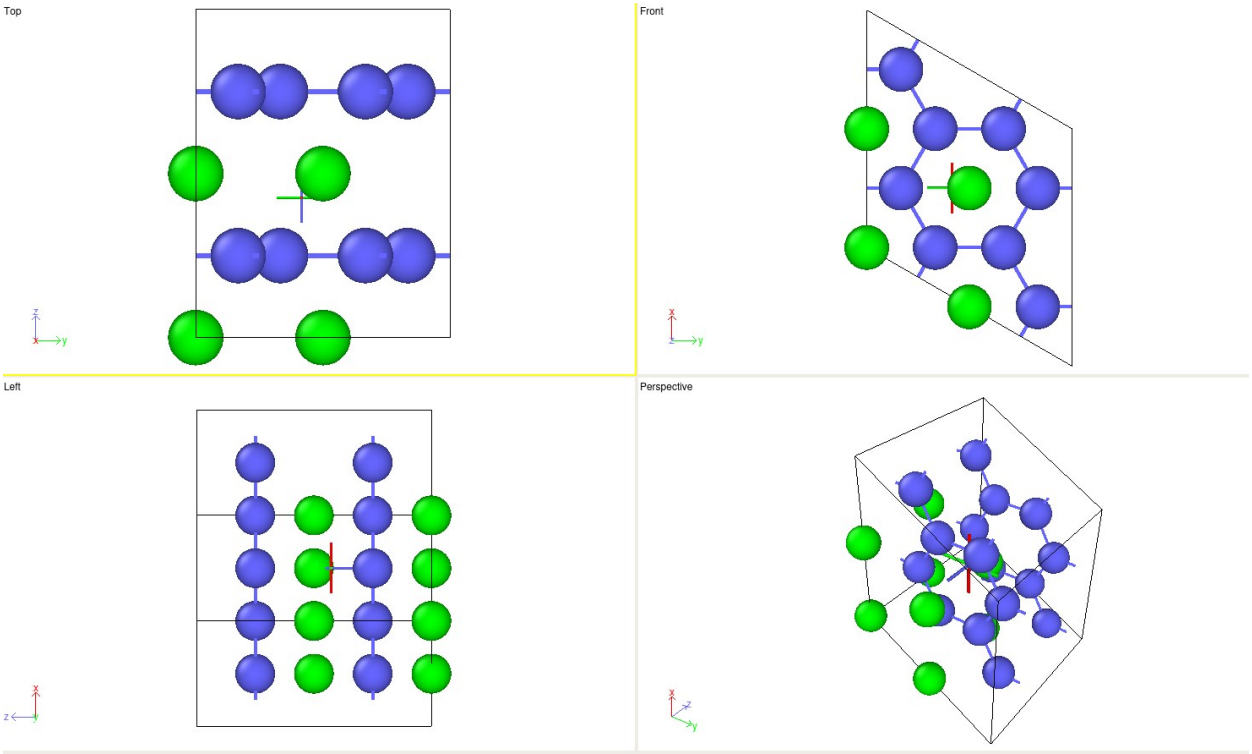

Figure 1. ZrB_2 crystal structure showing P6/mmm symmetry.

B-B bond strength contributes to the strength, hardness, and stiffness of ZrB_2, and Zr-B bonds formed by zirconium contributing two electrons and each boron atom in the unit cell sharing one electron contribute to the melting temperature. In addition, the thermal and electrical conductivities of ZrB_2 are aided by the remaining free valence electrons in the Zr-Zr plane.

Electrical Properties

Resistivity. Resistivity is the ability of a material to resist current flowing through it. According to the Drude model [12], resistivity is given by.

$$\rho = \frac{(m)}{(ne^2\tau)} \quad (1)$$

where m is the mass of an electron, n is the density of electrons, e is the electron charge and τ is the relaxation time. Here resistivity is directly proportional to mass as mass determines the acceleration in an electric field. As the number of electron carriers increases then resistivity decreases. There is no scattering of electrons in the perfect lattice but there is always a disruption of lattice mainly due to two factors:

a) All static imperfections such as impurities, defects, etc.

b) Lattice vibrations of ions around their equilibrium positions due to thermal excitation of ions.

As these two-mechanism act independently, the relaxation time of electron is given by.

$$\frac{1}{\tau} = \frac{1}{\tau_1} + \frac{1}{\tau_2} \quad (2)$$

Where the first term is due to static imperfections which is temperature independent, and the second term is due to lattice vibrations which depends on temperature.

From Eq. 1 and 2, we get,

$$\rho = \rho_i + \rho_{ph} \quad (3)$$

$$\rho = \frac{m}{ne^2\tau_i} + \frac{m}{ne^2\tau_{ph}} \quad (4)$$

Scattering by phonons is insignificant at very low temperature because the amplitude of lattice vibrations is small. Thus, at low temperature the resistivity is mainly due to static imperfections. Scattering of phonons became effective at high temperature, so ρ_{ph} increases. At very high temperature, the resistivity is mainly due to scattering by phonons as $\rho = \rho_{ph}$.

Resistivity of Ceramics. The electrical resistivity of ceramics is very low in the order of μΩ, so they are good conductor of electricity as well as have high thermal conductivity. Electrical resistivity of pure ZrB_2 as a function of temperature is shown in Figure 2 [6]. According to [6], the resistivity of ZrB_2 was observed to be 7.3 μΩcm at room temperature and increases

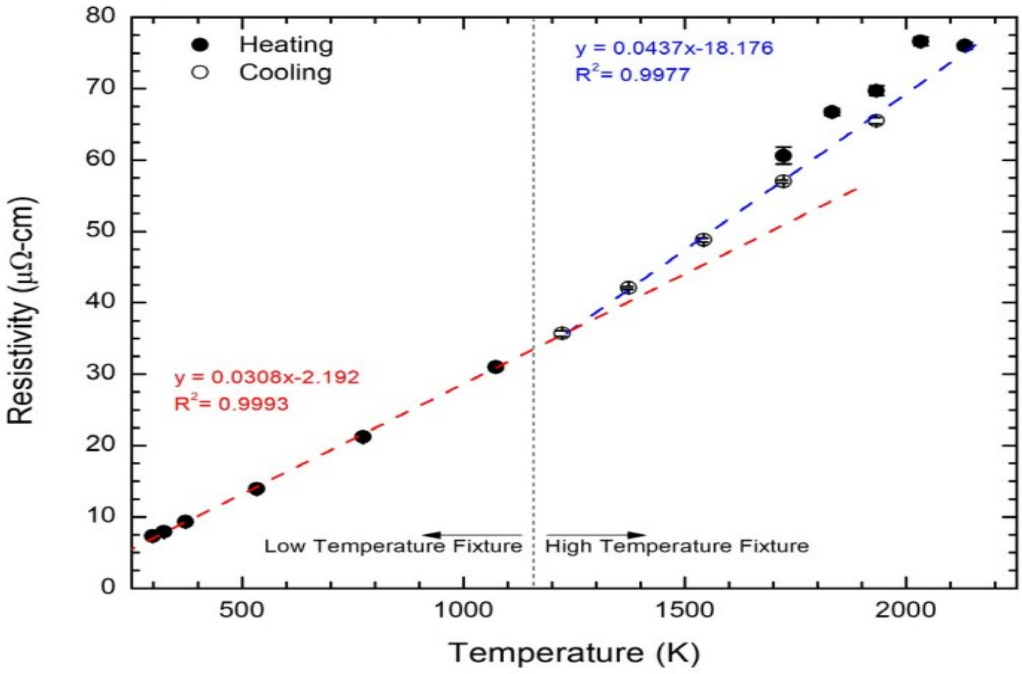

Figure 2. Resistivity of pure ZrB_2 with temperature [6].

linearly with rise in temperature up to 1223 K, and above 1223 K resistivity of ZrB_2 increases with greater slope. Based on previous works [10,13] on resistivity of ZrB_2, the shift in slope of electrical resistivity as a function of temperature was not expected. Several researchers [10,13] found out that the resistivity is proportional with temperature as shown in Figure 3. Neuman et al [6] reported that the change in the slope may be due to change in electron distribution with temperature or change in solubility of impurities with temperature.

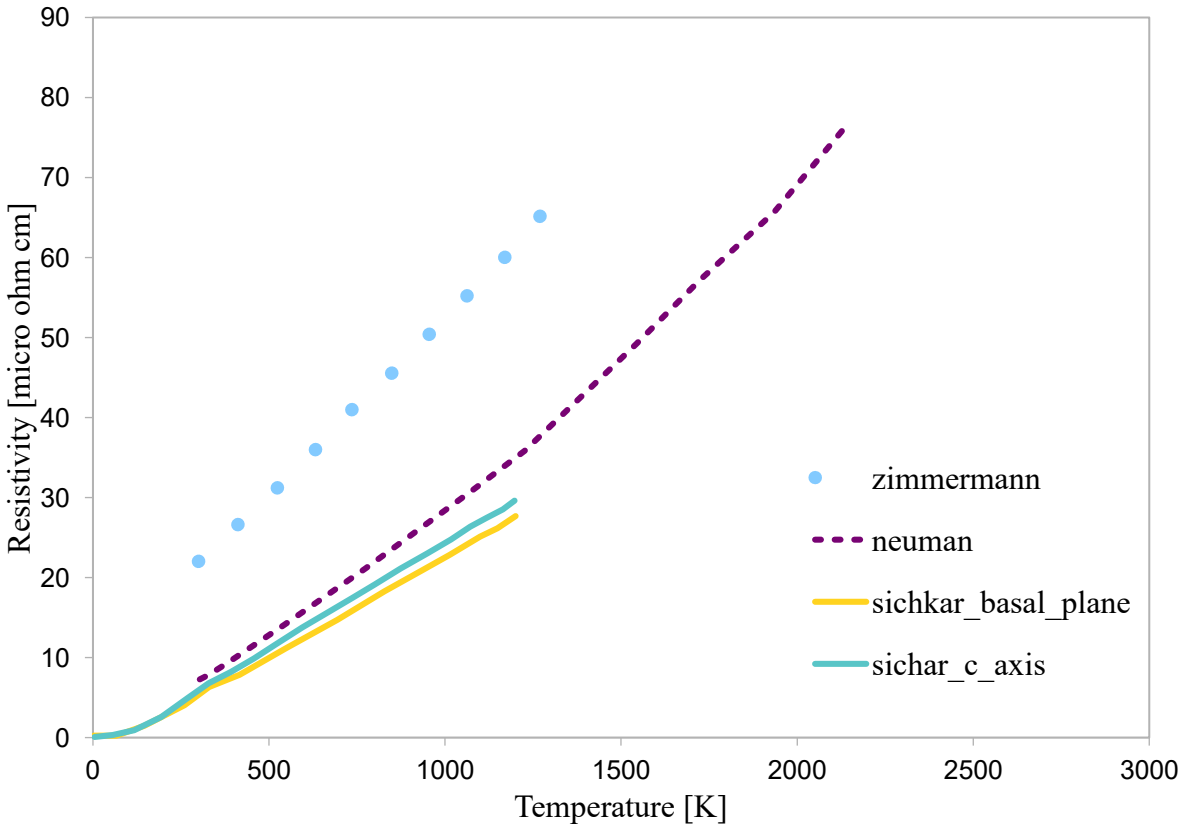

Figure 3. Resistivity of ZrB_2 of previous works [10,13].

Resistivity of ZrB_2 containing solid solutions. Various research has been carried out to increase the thermal conductivity of ZrB_2. McClane et al. [14] and Stanfield et al [15] predicted the resistivity of ZrB_2 containing solid solutions of different transition metals like Ta, Cr, Nb, Y, etc.

According to their reports [14,15], adding solid solutions of transition metals increases the resistivity in every case, and greatest effect is obtained by adding solid solutions of Cr to ZrB_2. As reported by McClane et al [14], addition of Cr at 3 at% increases the resistivity of ZrB_2 by more than 500%. The resistivity of ZrB_2 containing solid solutions of Cr, Ta, Mo, V and Re calculated by previous researcher [14] is shown in Figure 4.

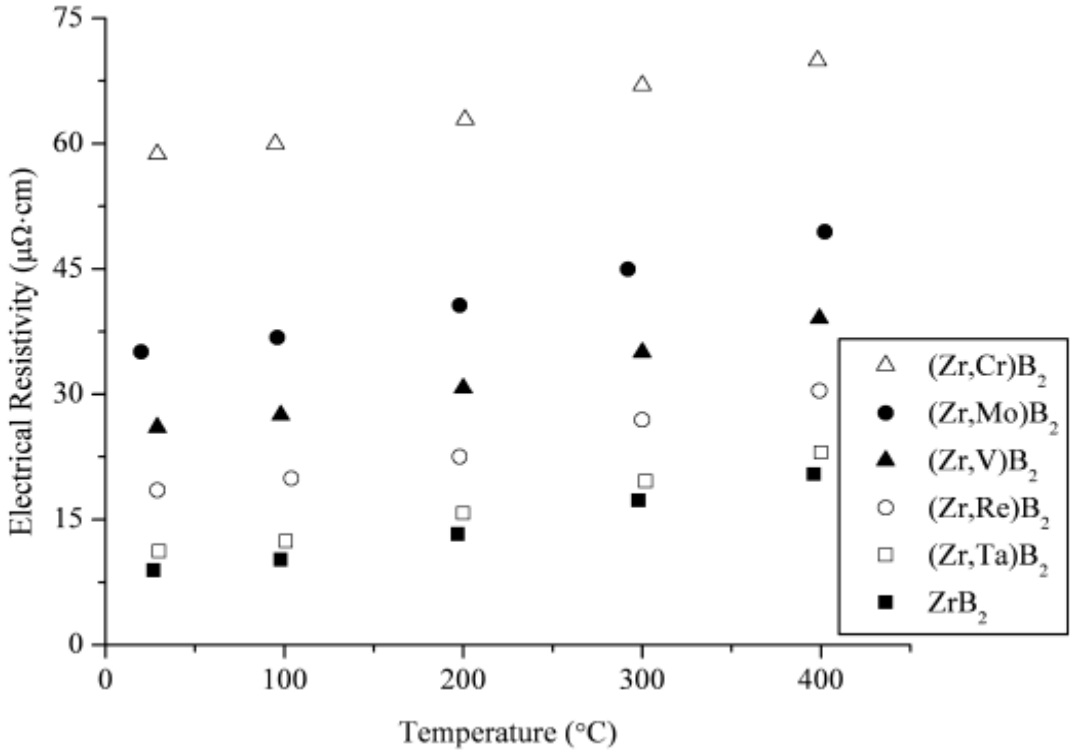

Figure 4. Resistivity of pure ZrB_2 and ZrB_2 containing solid solution of Cr, Mo, V, Re and Ta [14].

Thermal Properties

Thermal conductivity. Thermal conductivity is the ability of matter to transfer or conduct heat. Basically, there are three ways in which heat can be transferred: conduction, convection, and radiation [16]. The rate of flow of heat is given by [16]

$$Q = -Kdt \tag{5}$$

where Q is the rate of flow of heat, K is the thermal conductivity and dt is the change in temperature. Transfer of heat is mainly due to electrons, phonons and photons known as electron conduction, phonon conduction and photon conduction respectively [17,18].

Phonon conduction. At moderate temperatures, transfer of heat energy between atoms in ceramics is due to the propagation of elastic waves [17]. The phonon thermal conductivity is expressed as [16–18],

$$k_{ph} = \frac{1}{3} c_v l v \tag{6}$$

where, c_v is the volume heat capacity of material, l is the mean free path of phonons and v is the average velocity of elastic waves or phonons. When there is periodicity in the lattice then phonons are scattered and mean free path is determined by each of this scattering process, so the effective mean free path is obtained from the reciprocal addition of mean free paths from all active scattering [17].

At high temperatures (above debye temperature [19]), umklapp scattering [20] dominates the mean free path of phonons in which the mean free path is inversely proportional to temperature due to which thermal conductivity also varies as $\frac{1}{T}$as specific heat and velocity is almost constant [17,18]. At temperatures below debye temperature [19], thermal conductivity is inversely proportional to T^3 [17,18]. At very high temperatures, thermal conductivity is independent of temperature [16].

Electron conduction. In ceramic materials, transfer of energy is also due to mobile electrons. The electronic contribution to thermal conductivity is given by wiedemann-Franz law.

$$\frac{K_e}{\sigma} = LT \tag{7}$$

where, K_e is the electronic part of thermal conductivity, σ is the electrical conductivity, L is lorenz number and T is the temperature. The Lorenz number (L) is supposed to be constant with value of 2.44×10^{8} $W\Omega K^{-}2$. But experiments [21,22] shows that Lorenz number is not same for all materials and is temperature dependent. This mechanism has significant effect at high temperatures (T>400K).

Photon conduction. In addition, at high temperature, heat can also be transferred through transmission and absorption of electromagnetic energy [18]. The photon contribution to thermal conductivity is given as [17]

$$k_{pt} = \frac{16}{3}\sigma n^2 T^3 l_r \tag{8}$$

where, n is the refractive index, l_r is the mean free path of photons responsible for transfer of heat and T be absolute temperature. For opaque bodies, photon thermal conductivity is negligible because $l_r \sim 0$ for opaque bodies [17].

Thermal conductivity of Ceramics. Sindeband and Neel were historically known for producing ceramics with low thermal conductivities, owing to their low densities of 85 and 70%, respectively [7].

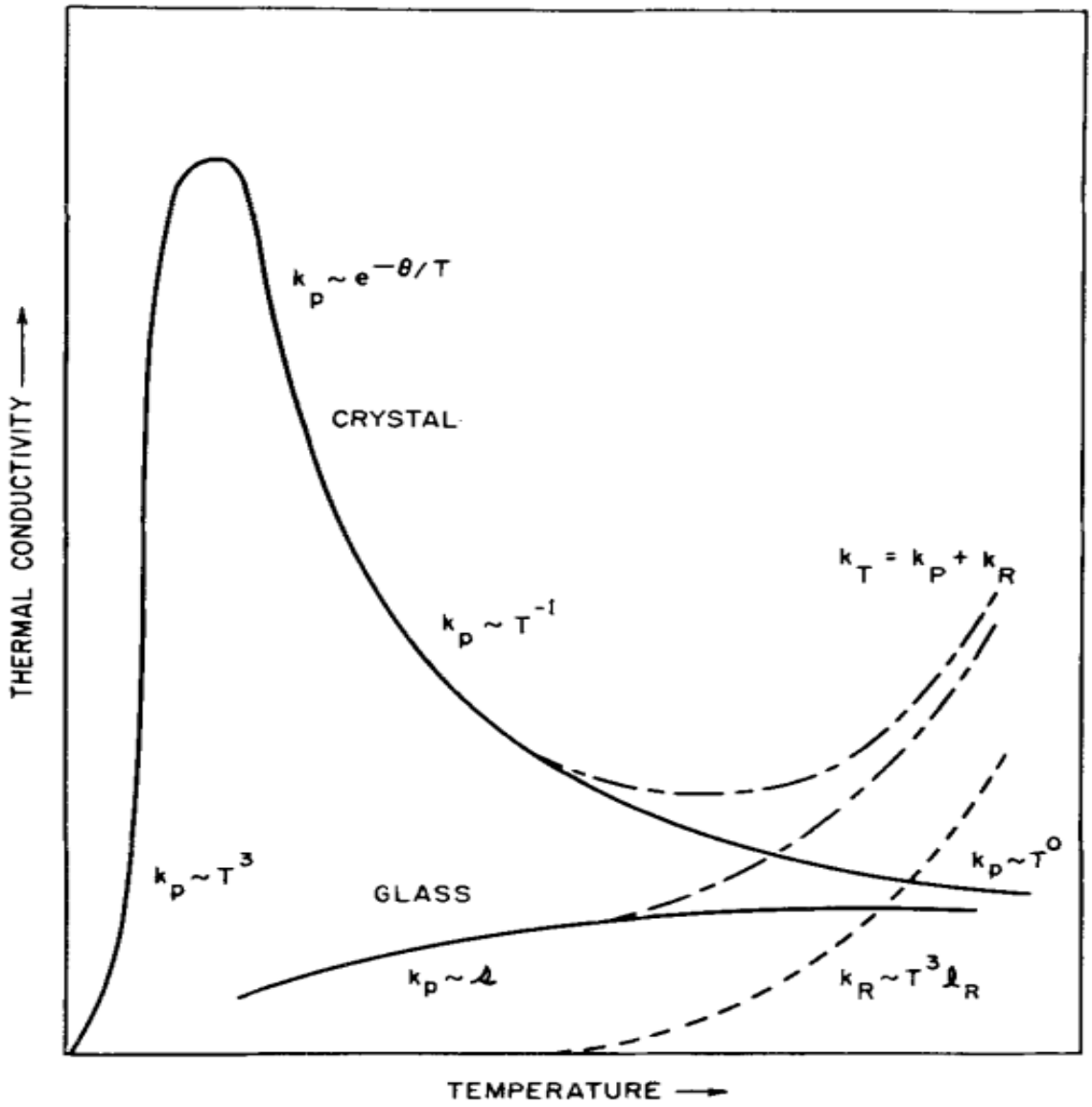

Figure 5. Thermal conductivity of crystal and glass [17,18]. K_{ph} and K_T are the phonon thermal conductivity and total thermal conductivity, respectively.

At high temperatures, the effect of density is practically noticeable, as k starts to rise as temperature rises, possibly due to the photon heat transfer due to the pores [7]. The thermal conductivity of different diborides like ZrB_2, TiB_2 and HfB_2 reported by previous work [23] are shown in Figure 6.

From Figure 6, these diborides are characterized as being conductive, with values equivalent to number of metals [13,23]. Furthermore, it was discovered that the electron contribution accounts for more than two thirds of the thermal conductivity of ZrB_2 [23–25].

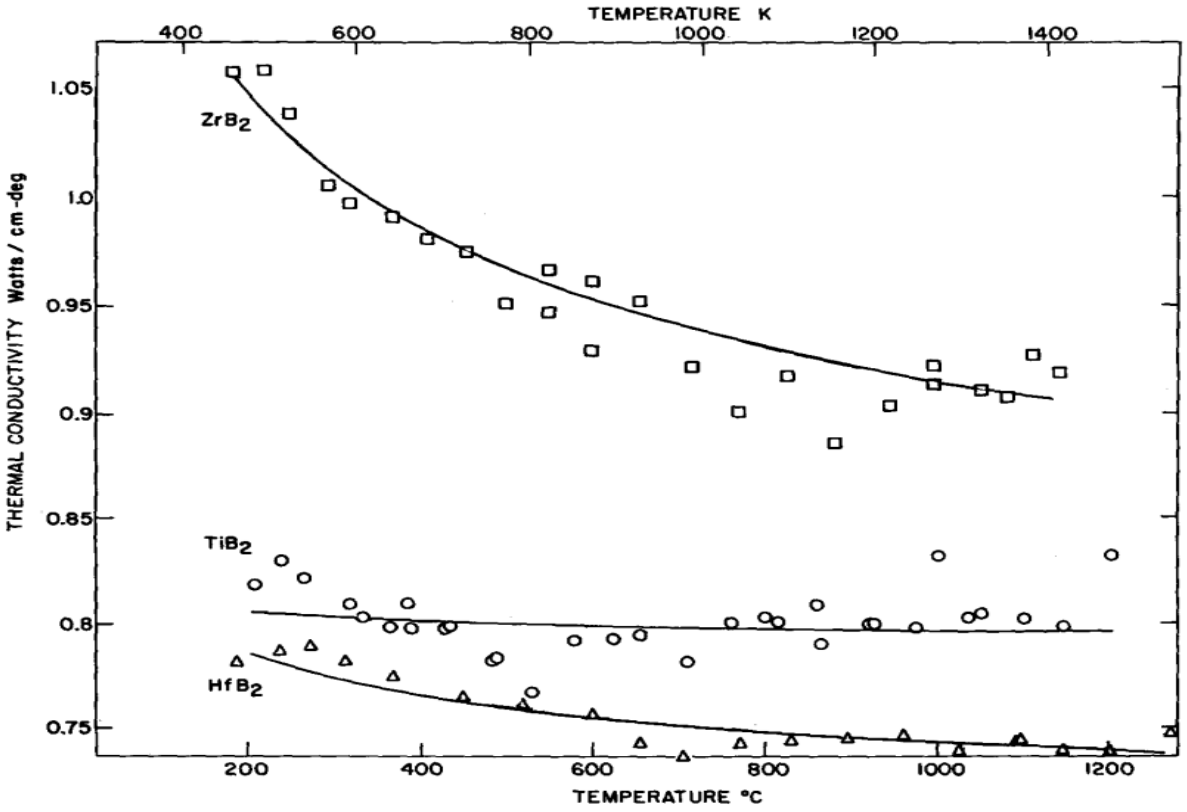

Figure 6. Thermal conductivity of ZrB_2, TiB_2 and HfB_2 from previous work [23].

Experimentally, thermal conductivity can be calculated using thermal diffusivity(D) and heat capacities (C_p) using the following equation.

$$k = DC_p\rho \tag{9}$$

where, ρ is the specimen density, which can be calculated using linear expansion using the equations.

$$\rho(T) = \rho_{300K}\left[1 + \frac{(\Delta l)}{l_{300}}\right]^{-3} \quad (10)$$

where Δl is experimentally calculated linear thermal expansion. Both electron and phonon contribution are included in the thermal conductivity calculated using equation 9**.** The electronic contribution to thermal conductivity can be calculated using wiedemann – Franz law as shown in equation 11.

$$K_e = L\sigma_e T \quad (11)$$

where K_e is the electronic thermal conductivity, L is the lorentz number (2.45 x 10^{-8} W Ω $K^{-}2$) and T is the temperature. Thermal conductivity and electronic thermal conductivity of ZrB_2 calculated by Zimmermann et al [13] is shown in the Figure 7.

Thermal conductivity of ZrB_2 containing solid solutions. To increase the thermal conductivity of ZrB_2, McClane et al [14] and Stanfield et al [15] dissolved solid solution of transition metals like Cr, Ta, Y, Nb, Hf, etc in ZrB_2. As a result, thermal conductivity, and electronic contribution to thermal conductivity of ZrB_2 decreases in every case. Variation of total thermal conductivity of ZrB_2 with solid solutions (3 at%) is shown in the Figure 8. The addition of transition metals decreased the electronic contribution to thermal conductivity, which followed the same general pattern as the overall thermal conductivity [14]. TM additions, on the other hand, reduced the electron contribution to thermal conductivity by a greater percentage than the overall thermal conductivity [14]. The electronic thermal conductivity calculated by McClane et al [14] is shown in Figure 9.

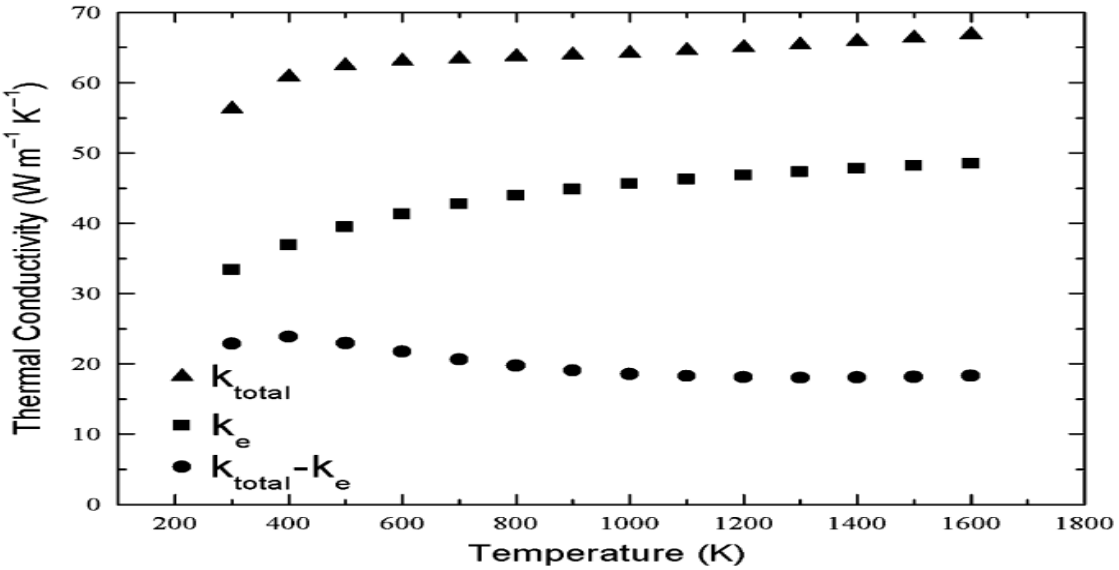

Figure 7. Total thermal conductivity with electron and phonon contribution of ZrB_2 [13].

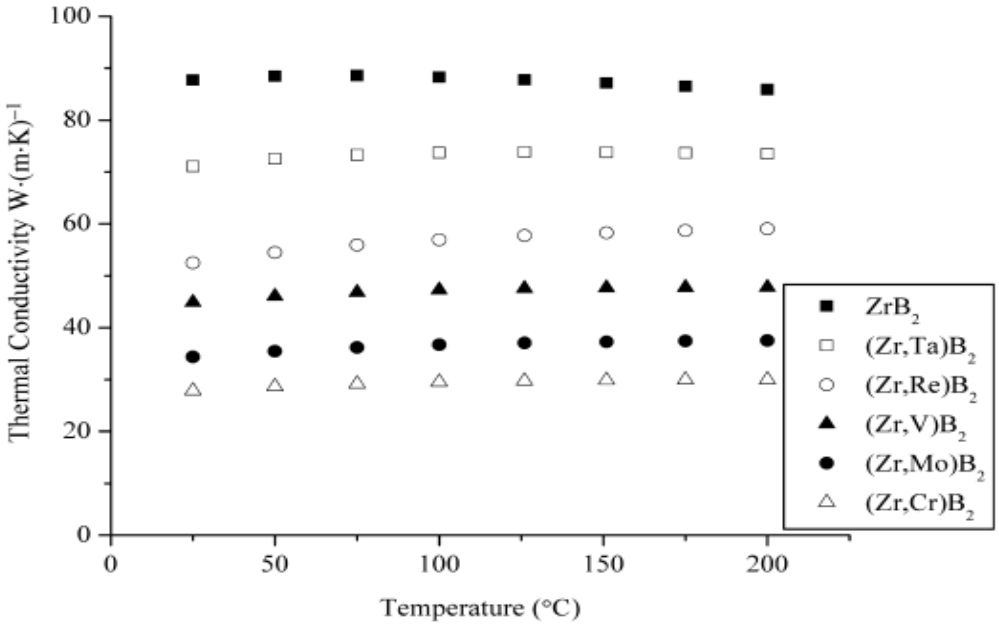

Figure 8. Total thermal conductivity of ZrB_2 and ZrB_2 containing solid solutions of Ta, Cr, Re, V and Mo [14].

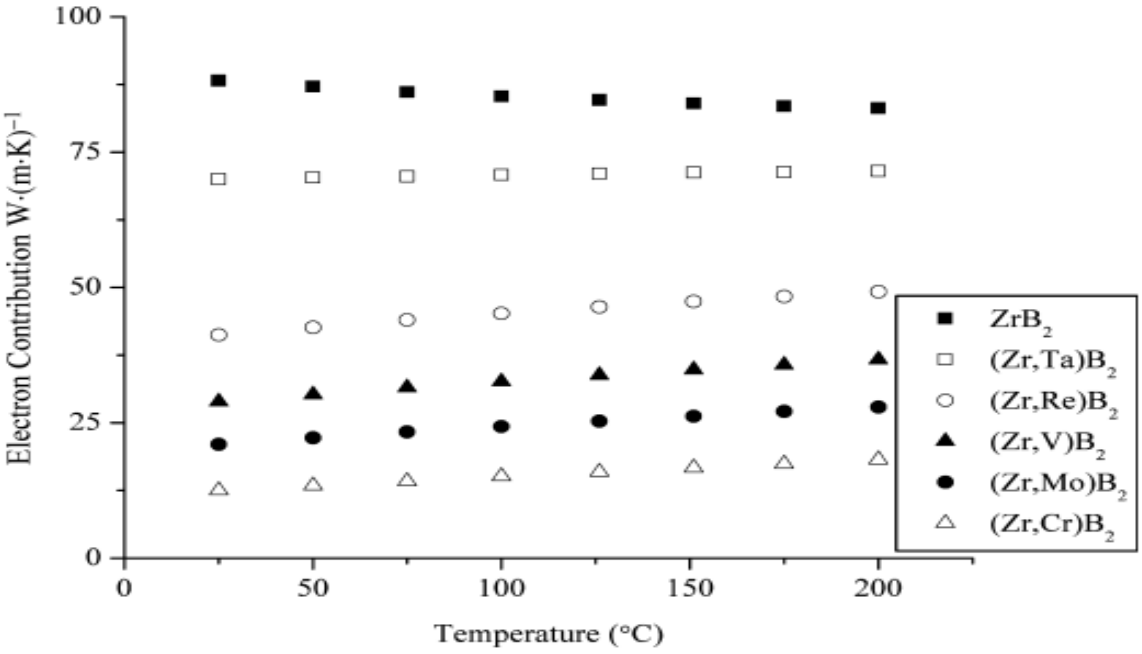

Figure 9. Electron contribution to thermal conductivity of ZrB_2 and ZrB_2 containing solid solutions of Ta, Re, V, Mo, and Cr [14].

Density Functional Theory

In theory, the quantum mechanical wavefunction, includes all the knowledge about a system. So, to get all details about a system, we should solve the schrodinger equation of a system. Unfortunately, it is not easy to solve the schrodinger equation of N body problems, so we should make certain approximations. Many traditions approach is developed to solve the schrodinger equation for N body problems. However, there are significant drawbacks like, with N, the computational effort increases very quickly, making the definition of larger system restrictive [26]. To overcome these limitations, a different approach is considered called Density functional theory which uses one-body density as a fundamental variable instead of many-body wavefunctions [26]. Kohn and Hohenberg proved two basic mathematical theorems that underpin the entire field of density functional theory [27]. They are:

1. The ground state energy from the schrodinger's equation is the unique functional of electron density.

2. The electron density that minimizes the energy of the overall functional is the true electron density corresponding to the full solution of schrodinger equation.

We would like to find the Schrodinger equation's ground state energy, but it is difficult task as it is many bodies issue. Kohn, Hohenberg and Sham's stunning finding demonstrated that the ground state we searched can be reached by minimizing the energy of the energy functional and seeking a self-consistent solution to a series of single particle equations [27]. Thus, Kohn, Hohenberg and Sham's theorem establishes the theoretical basis for creation of efficient single particle scheme for calculating the ground state density and energy of the electronic system [26]. To solve the Kohn-Sham equation, we must specify the exchange correlation functional which is not that easy. Although, DFT does not provide any guidance on how to build approximate exchange-correlation functional, it does promise and challenge that the true exchange-correlation functional is the universal density functional, that is, it has the same functional form for all the systems [26].

One of the approximations for energy correlation functional is Local Density approximation (LDA). A real inhomogeneous system is divided into infinitesimal volumes in this method, and the electron density in each volume is assumed to be constant [28]. The exchange-correlation energy obtained from the uniform electron gas for that density is then assumed to be exchange-correlation energy for the density of each volume [28]. In LDA, the exchange-correlation function is given as

$$E_{XC} = \int n(r)\, e_{xc}^{uni} n(r) d^3(r) \qquad (12)$$

Where, $e_{xc}^{uni}(n(r))$ is the exchange-correlation energy per particle of an electron gas with spatially uniform density n(r) [26]. The LDA is a good approximation for spatially gradually evolving densities attributable to its design. Even though this requirement is rarely met in real-world electronic system, LDA has proven to be surprisingly accurate for a wide range of application [26]. Recent research [29–31] have shown that for metals and insulators, LDA appears to overestimate cohesive energies by 15-20% and underestimates lattice constants by 2-3%.

The fact that only the local uniform density at each given point is not a rational approximation for the rapidly changing electron densities of several materials were recognized early on, and the gradient of density n(r) should be included. The advent of so-called generalized gradient approximation (GGA) provided a significant advance in the search for better functionals [26]. GGAs can outperform LDA for variety of properties, such as geometry and ground state energies of molecules and solids. Within GGA, the exchange-correlation energy takes the form [28],

$$E_{XC} = \int n(r)\, e_{xc}^{uni} n(r) F_x^{GGA}(s) d^3(r) \qquad (13)$$

where F_x^{GGA} is the exchange enhancement factor and tells how much the exchange energy is enhanced over its LDA value at given n(r) [28]. One GGA varies from another depending on the F_x^{GGA} used. S is the dimensionless reduced gradient given by [28].

$$s = \frac{\Delta n(r)}{2(3\pi^2)^{\frac{1}{3}} n(r)^{\frac{4}{3}}} \qquad (14)$$

In calculation involving solids, most widely used GGAs functional are Perdew-Burke-Ernzerhof (PBE) and Perdew-Wang (PW91) functional [27]. Our definition of GGAs functional as involving information from the electron density and its gradient implies that more complex

functional based on other pieces of physical information can be produced. In our calculations, we used PBE exchange-correlation functional to find the ground state energy of the diborides.

The basis for the single-particle wave functions must be chosen after the exchange correlation potential has been selected. Invoking Bloch theorem to express the wavefunction as the periodic Bloch function multiplied by the complex phase factor, whose wavevector is taken from the first Brillouin zone of the reciprocal lattice, the inherent periodicity of a crystal can be exploited [32]. Bloch functions sampled on the discrete mesh of wave vectors known as k-points are used to estimate integrals over the Brillouin region numerically. Since Kohn-Sham states differ smoothly, a well converged sampled density can typically be achieved with a small number of wavevectors in semiconductors and insulators [32]. The sudden shift in the occupancy of each state with wavevector, on the other hand, necessitates much denser grids for metals. Bloch functions can be represented as an expansion in terms of a series of mathematical basis functions, with the coefficient of these function serving as the primary values of constructing a computational representation. Different basis sets have been created, the most common of which is the plane-wave basis set. Each Bloch state is represented by Fourier series with plane waves as basis sets and reciprocal lattice vector as wavevector [32]. The merits of plane wave basis sets over other basis sets are [32],

a) It represents the periodicity of ordered material.

b) It allows matrix elements to be computed conveniently and concisely.

c) It is an orthonormal basis set.

d) A single parameter, cut off energy E_{cut} or equally wavevector G_{cut}, controls its size and precision.

Since the ground state energy varies with G_{cut}, it is possible to increase accuracy by simply increasing G_{cut}. The key drawback is that, as compared to localized basis sets, the number of basis functions needed is high, which increases computational cost, which is a particularly serious problem for the evaluation of the Fock exchange term as required by hybrid exchange-correlation functionals. The second challenge is representing sharp peaks in Kohn–Sham states, such as those found near nuclei in the core regions. The electron–nuclear Coulomb attraction is singular in the core regions, and it is this singularity that causes the strong wavevector, sharp peaks in the Kohn–Sham states [32]. In these core regions, the Coulomb interaction dominates the potential, and the shape of the Kohn–Sham states near a nucleus is almost entirely independent of the chemical environment. Because of this environmental independence, states in the core area have a negligible impact on a material's chemical or electronic properties, and it is unnecessary to reflect them or the Coulomb potential precisely [32].

The Kohn–Sham equations must be solved to determine the plane-wave coefficients of single-particle wave functions. These Schrödinger-like equations are eigenvalue equations that could theoretically be solved by directly constructing the Hamiltonian and diagonalizing it (as is often done in localized basis set methods) [32]. The Hamiltonian, on the other hand, is a density functional, and the density is determined by wave functions. The Kohn–Sham equations are transformed into nonlinear eigenvalue equations by the Hamiltonian's implicit wave function dependency. Iterative diagonalization methods [33] can be used to find the solution to these nonlinear eigenvalue equations instead of solving them directly. The self-consistent field (SCF) method, in which the nonlinearity of the Kohn–Sham eigenvalue equations is removed by solving them for a given, approximate input Hamiltonian, is a popular method of solution. The resulting Kohn–Sham states produce a particle density that is inconsistent with the input

Hamiltonian in general, but this density can be used to compute an improved approximate Hamiltonian and the states recalculated. This process can be repeated until the Hamiltonian changes are marginal, the measured states and Hamiltonian are (approximately) self-consistent, and the algorithm has converged to the ground state solution.

Pseudopotential. It is well known that the valence electrons, rather than core electrons, define most physically interesting properties of solids. Meanwhile, the definition of deeply bound core electrons in plane-wave basis sets necessities many basis functions [28]. As a result, the less critical core electrons will absorb a large portion of the computational expense. The pseudopotential approximation solves the problem by replacing the high ionic potential with the pseudopotential.

The pseudopotential formalism has two general-purpose in general [28]: to begin, a much weaker pseudopotential was used to exclude core electrons, which would otherwise have to be represented by many plane-wave basis functions due to their deep potential. Second, in the core area, to remove the rapid oscillations of the valence electron wave functions. These problems are illustrated in Figure 10**,** where the pseudopotential is much weaker than all-electron one, and the pseudo function has no pseudo node within the core field [28]. It is important in the pseudopotential scheme that the pseudopotential and the wavefunction outside the core region match the corresponding all-electron ones.

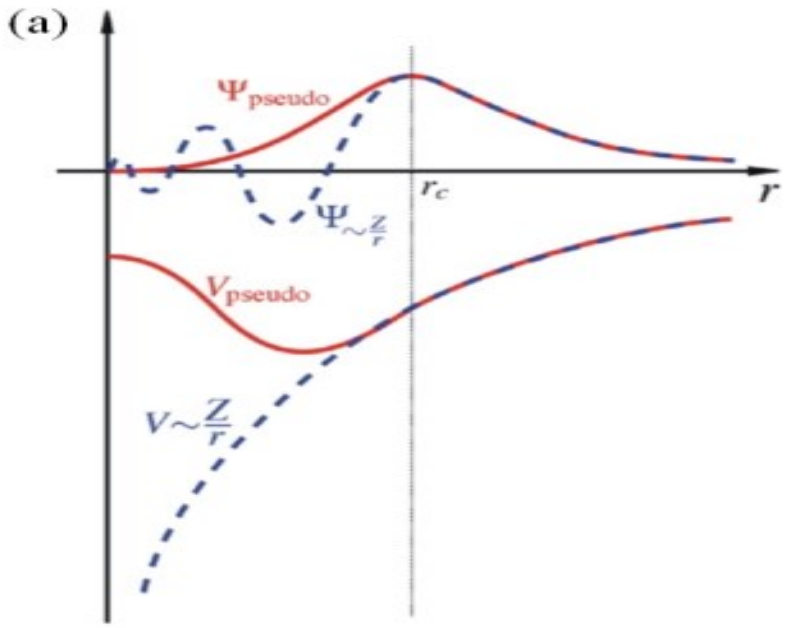

Figure 10. Schematic illustration of all-electron (dashed lines) and pseudopotential (solid lines) and their corresponding wavefunctions [28].

In general, a pseudopotential replaces the electron density of specific group of core electrons with a smoothy density that matches the true ion core's significant physical and mathematical properties. The frozen core approximation fixes the properties of core electrons in all subsequent calculations in this approximate manner. All-electron measurements are those that do not use a frozen core and are used even less often than frozen core approaches. In an ideal world, a pseudopotential can be created by considering an isolated atom of one element, but the resulting pseudopotential could be used reliably in calculations that position this atom in any chemical environment without the need of the further pseudopotential adjustment [27]. The transferability of the pseudopotential is the name of this valuable property [27]. Typical DFT codes contain library of pseudopotential with entries for each (at least majority) elements of the

periodic table. The specifics of the pseudopotential describe a minimum energy cutoff that should be used in calculations involving atoms with that pseudopotential. Hard pseudopotentials need high energy cutoffs, while soft pseudopotential needs low energy cutoffs and are more effective [27]. The ultrasoft pseudopotential (USPPs) are the most used pseudopotential. These pseudopotentials, as their name implies, need significantly lower cut off energies than alternative approaches. One downside of using USPPs is that constructing the pseudopotential for each atom necessitates the specimens of variety of important parameters [27]. Current DFT codes usually only contains carefully design and checked USPPs, but they do sometimes include several USPPs with varying degree of softness for certain components. The projected augmented-wave (PAW) process, first introduced by Blochl, later adapted for plane wave calculations by Kresse and Joubert, is another frozen core approach that avoids some of the drawbacks of USPPs. For small molecules and extended solids, Kressa and Joubert USPP, PAW and all-electron calculations [34]. Their findings shows that well-constructed USPPs and PAW method produces virtually similar results in certain cases, and that these results agree well with all-electron calculations. The PAW method is more reliable than USPPs in materials with high magnetic moments or atoms with significant variation in electronegativity. In our research, we used PAW Pseudopotentials for diborides.

Wannier Functions. The reciprocal lattice in a perfect crystal has a periodicity such that the electric potential at either point in the lattice should be the same as the corresponding point in an adjacent Brillouin field, implying that the electric potential has the same periodicity as the lattice. Consider the translation vector **R,** which is defined as an operator that moves the Hamiltonian one cell in the r-th direction. Then

$$\mathbf{RH = HR}$$

Then the Bloch functions is defined as [35–37],

$$\psi_{nk}(r) = U_{nk}(r)exp(ik.r) \quad (15)$$

where U_{nk} has the same periodicity as the electric potential, r is the real-space location, k is the Brillouin zone wave vector, n is the band number, and $exp(ik.r)$ is referred to as an envelope function [36]. The states $\psi_{nk}$is defined for every n, so that $\psi_{nk}$is the eigenstates of Hamiltonian.

The electronic ground state of solids with periodic boundary conditions can be expressed in terms of Bloch orbitals, which are labeled by their location in reciprocal space and their energy band or bands [35,36]. These Bloch orbitals are energy localized in the sense that they are the Hamiltonian eigenstates. The overall step and gauge preference of the Bloch orbitals are indeterminate, which means that any arbitrary unitary transformation of the Bloch orbitals would produce the same physics. The Wannier functions, a superposition of Bloch orbitals determined via a sequence of unitary transformations proposed by Gregory Wannier in 1937 [38], can then be expressed. The envelope function generates a separate wave function for each k, and since the sine and cosine functions, and thus the Bloch functions, are orthogonal, we should be able to generate additional wave functions by superimposing two or more Bloch functions [36,37]. A localized wave packet is one such potential wave function that should be predicted. We begin by super positioning every Bloch feature in the Brillouin zone to create these.

$$w_0(r) = A\int \psi_{nk}(r)dk \quad (16)$$

where w_0 is the wannier function and A is the normalization factor [37]. In the same way as similar orbitals, known as localized molecular orbitals, are used in chemistry to find a description that belongs to each individual molecule and are approximately translational images of the localized molecular orbitals of other molecules, Wannier functions can be found that belong to a

single cell in a solid, where the Wannier function of each cell is the translational image of the Wannier function of other cells [36]. Owing to the indeterminacy of the Bloch orbitals, these Wannier functions are strongly non-unique, and the obvious alternative is to use the Wannier functions that are maximally localized [35,36,39].

METHODOLOGY

To model the crystal structures, structure relaxations were firstly performed using the DFT code of VASP [40,41] which allows for rapid and efficient convergence. In VASP, Plane Augmented wave (PAW) pseudopotentials were used for both Zr and B, with $4s^2 4p^6 4d^2\ 5s^2$ valence electrons for Zr and $2s^2 2p^1$ valence electrons for B. The dimensional and internal position data of the relaxed crystal structure were then used as initial inputs for the remaining DFT calculations using the Quantum Espresso (QE) code. The structural relaxations from VASP were repeated. In QE, an LDA exchange correlation functional was used [42]. The optimized lattice parameters of metal diborides are shown in Table 1.

Density of States

The number of states in a small interval near a given energy is given by the density of states, which is a compact representation of the electronic structure. Density of states (DOS) of pure diborides were calculated using tetrahedron method with 12x12x12 Kpoints and electrons convergence threshold of 10^{-9} Ry. The pseudopotential used for all diborides is shown in Table 2. Self-consistent calculations were performed with kinetic energy cutoff of 45.55 Ry and $12x12x12$ k points. Non-self-consistent calculations used $45x45x45$ k points with same criteria for energy minimization. The fermi energy obtained for ZrB_2, CrB_2, TiB_2, AlB_2 and TaB_2 are 15.9272, 17.1032, 14.9155, 11.6535 and 21.5719, respectively.

A 2x2x2 supercell of ZrB_2 for the doped diborides was made, which contains 8 Zr atoms and 16 B atoms, totaling 24 atoms. After that, one Zr atom (in the center) is replaced with one TM (Al, Ta, Cr) atom. Figure 11 shows the crystal structure of ZrB_2 doped with a TM atom.

Ground state measurements for doped diborides were done with an electron convergence threshold of 10-6 Ry and 4x4x3 Kpoints. With the relatively larger number of atoms i.e., a larger supercell, a smaller number of Kpoints can be used since the Brillouin zone (BZ) in reciprocal space accordingly will be smaller. Non-self-consistent calculations were determined with 15x15x15 Kpoints with same criteria of energy minimization.

Table 1. Lattice parameters of respected Diborides

Metal Diborides	Lattice parameter (a)	Lattice parameter (c)
ZrB_2	3.162	3.531
TiB_2	3.035	3.223
CrB_2	2.957	3.029
TaB_2	3.093	3.336
AlB_2	3.006	3.274

Table 2. Pseudopotential of diborides

Elements	Pseudopotential type	Pseudopotential
Zr	Plane augmented wave	Zr.pbe-spn-kjpaw_psl.1.0.0.UPF
Ti	Plane augmented wave	Ti.pbe-spn-kjpaw_psl.1.0.0.UPF
Cr	Plane augmented wave	Cr.pbe-spn-kjpaw_psl.1.0.0.UPF
Ta	Plane augmented wave	Ta.pbe-spfn-kjpaw_psl.1.0.0.UPF
Al	Plane augmented wave	Al.pbe-n-kjpaw_psl.1.0.0.UPF
B	Plane augmented wave	B.pbe-n-kjpaw_psl.1.0.0.UPF

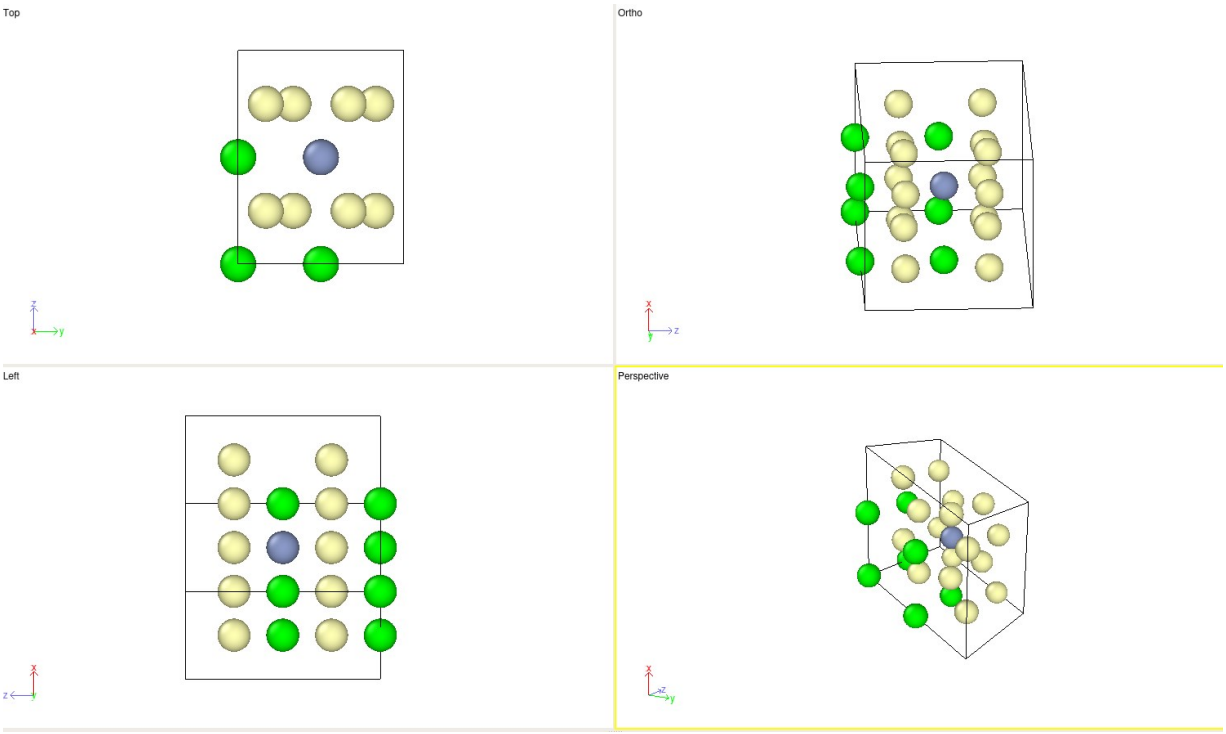

Figure 11. Crystal Structure of ZrB_2 doped with Cr. Green, yellow and Grey represents Zr, B and Cr atoms, respectively.

Electrical Resistivity

The transport properties of an electron gas can be modeled by describing the distribution function of electron gas. In this context, the Boltzmann transport equation (BTE) has been established to obtain the above distribution function to account for the presence of external forces. The BTE relates the variation in the carrier distribution (occupied energy states) to forces that drive the carrier to a non-equilibrium state and describes the transport of charge carriers [8,31]

$$\left(\frac{\partial f}{\partial t}\right)_{scattering} = -\left[\frac{\partial f}{\partial E_k} v_k e E\right] \quad (17)$$

Where E is electric field, f is force, t is time, e is electrical charge, v_k is velocity at state k. In this form, the left side of equation 17 describes the distribution function due to all the active scattering mechanisms like phonon-phonon scattering, electron-phonon scattering, impurity

scattering, etc. The relaxation time τ between scattering events must be estimated *a-priori* to derive an analytical solution of equation 17. Here, a simplified model can be made for the relaxation time as the average time between two successive collisions, where the carriers are driven from an excited state to an equilibrium distribution. The frequency of collisions, $\tau^{-1}(E)$ would thus, only be dependent on the density of states, g(E), which can be quantitatively extracted from the DFT calculations. Following the approach by Poncé et al. [32], the temperature dependence of resistivity can then be approximated using the Ziman resistivity formula:

$$\rho(T) = \left(4\pi \frac{(m_e)}{(ne^2 K_B T)} \int \; dw\,(hw) \right) \alpha^2_{tr} F(w) n(\omega, T)[1 + n(\omega T)] \tag{18}$$

Where m_e is the mass of electron, n is the number of electrons per unit cell, $\alpha^2_{tr}\,F(w)$ are transport spectral functions, K_B is Boltzmann constant, T is temperature, h is planck constant, w is angular frequency and n(w,T) is the Bose-Einstein distribution. The low (below 300K) temperature electrical resistivity can be attributed to a variety of factors namely the electron-electron interactions, size effects, scattering from impurities, etc. [33]. The approximation to the solutions of the BTE in equation 17 can be used to estimate the electrical resistivity [32].

The electrical resistivity and electron-phonon lifetimes were then calculated using Electron-Phonon Wannier (EPW) code [43] which was interfaced with QE. The ground state is first calculated using Marzaari-vanderbilt smearing and a force convergence threshold of 1d-4 Ry with 12x12x12 Kpoints. For the phonon calculations, $12x12x12$ k-points with the force convergence threshold of 1.0d-4 Ry were used. Dynamical matrix in irreducible gamma centered $6x6x6$ q-points were calculated. To calculate electron phonon interactions, 216 k points were used, and the projection of orbitals are based on their respective valence electrons. 5 wannier functions were determined for all diborides along the G-X-W-L-K-G direction, with 5 CG steps

before reset and a 10d-9 Ry convergence tolerance. Finally, resistivity of diborides is calculated from 0 to 2500K. The input parameters for the calculation of resistivity are shown in appendix.

Normalized Conductivities

Thermal conductivity, Seeback coefficient, and electrical conductivity were then calculated following the Boltzmann transport theory as implemented in the BoltzTrap code [44]. The conductivity tensors are calculated by solving the BTE using relaxation time approximations where electrical conductivity per relaxation time is given as [34]

$$\sigma_{el} = \frac{1}{v}\int d\varepsilon\,(-f)\Sigma v_{\lambda} x v_{\lambda} \tau_{\lambda} \delta(\varepsilon - \varepsilon_k) \tag{19}$$

where λ include wave vector and band quantum numbers λ≡{n,k}, f'=d_{ε}f(T,ε) is the electron occupancy energy derivative, v_{λ} is the band velocity tensor, V is the volume of the unit cell and τ_{λ} is the electron relaxation time.

As seen in Table 2, the same diboride pseudopotential is used. The 10-6 Ry force convergence threshold and 12x12x12 Kpoints are used to calculate the ground condition. For Kohn-Sham Staes $24x24x24$ k points were taken for non-self-consistent calculations with the same basis set as that in QE. The transport properties were calculated based on relaxation time approximations of BTE at a temperature range of 0-2500 K. Thermal conductivities and electrical Conductivities obtained by this process are in the function of chemical potential and temperature. From the electrical resistivity obtained from EPW code and conductivity per relaxation time from BoltzTrap code, relaxation times for each metal diborides were obtained, which were subsequently used to in the prediction of the total thermal conductivities of other metal diborides.

Lattice Thermal Conductivity

The Linearized Boltzmann Transport Equation (LBTE) [45] is used to estimate lattice thermal conductivity. However, the complete solution of LBTE, as seen in [46], is very expensive. As a result, several approximations are made, one of which is the single mode relaxation time approximation (SMRT). Using this approximation, the lattice thermal conductivity can be written as [47],

$$K = \frac{1}{NV_0}\sum c_\lambda v_\lambda \otimes v_\lambda \tau_\lambda^{SMRT} \quad (20)$$

where, V_0 is the volume of unit cell, v_λ is the group velocity of phonon mode λ, τ_λ is the SMRT of the phonon mode λ [47]. C_λ is the mode independent heat capacity defined as [47],

$$C_\lambda = K_B\left(\frac{h\omega_\lambda}{K_B T}\right)\frac{exp\frac{h\omega_\lambda}{K_B T}}{\left[exp\left(\frac{h\omega_\lambda}{K_B T}\right)-1\right]^2} \quad (21)$$

where K_B is the Boltzmann constant, h is the reduced planck constant, ω_λ is the harmonic frequency of phonon mode λ and T is the temperature. It is also assumed in this procedure that phonon relaxation time is determined by phonon lifetime [47].

Lattice thermal conductivity was computed using the second order perturbation theory implemented in Phono3py [47], which calculates lattice thermal conductivity by solving linearized phonon Boltzmann transport equations with a single mode relaxation time approximation [47]. The Vienna Ab-initio Simulation Package (VASP) [40,41] was used to perform the density functional theory (DFT) calculations in this study. The GGA exchange correlation functional described by Perdew, Burke, and Ernzerhof [48,49] was used in conjunction with the projector augmented wave (PAW) potentials [50].

For ionic relaxation of all pure diborides, conjugate gradient algorithm (51) was used, and the convergence threshold of forces are set to be 0.02 ev. The cut off energy was set to be 275 ev for all pure diborides with Gaussian smearing with a width of 0.1 ev. For pure diborides, forces are calculated for 188 displacements which are made from 2x2x2 supercell. For the calculation of ZrB_2 doped with Cr at 12.5%, the cut off energy of 520 ev was used and 1080 displacements were made from 2x2x2 supercell.

Scattering rates and Mobility

The drift and collision factors in the BTE balance out over time in the presence of an external electric field; the field forces the electron distribution out of equilibrium, while collisions attempt to restore it. A nonequilibrium electron distribution is obtained at steady state, and the BTE as shown in equation 1 becomes.

$$\frac{-eE}{\hbar}.\Delta_k f_{nk}(t) = I^{e-ph}[f_{nk}] \tag{22}$$

where $f_{nk}$is the electron occupation with crystal momentum k and spatial coordinate r, E is the electric field and $I^{e-ph}$is the collision integral due to electron phonon scattering [52,53]. The steady-state electron distribution deviates very slightly from its equilibrium value when the electric field is relatively modest. The first order deviation from equilibrium of the electron distribution is given by [52]

$$F_{nk} = \tau_{nk} v_{nk} + \frac{\tau_{nk}}{N_q} \Sigma_{m,vq} F_{mk+q} W^{vq}_{nk,mk+q} \tag{23}$$

where $v_{nk}$is the velocity and $\tau_{nk}$is the electron relaxation time which is calculated as an inverse of scattering rate (Γ^{nk}). The scattering rate is given by [52]

$$\Gamma^{nk} = \frac{1}{N_q} \Sigma_{m,vq} w^{vq}_{nk,mk+q} \tag{24}$$

where $W_{nk,mk+q}^{nq}$involves both phonon emission and absorption processes [52]. After F_{nk} has been computed, the conductivity tensor can be computed using the following relation [52]

$$\sigma_{nk} = \frac{1}{\Omega E_\beta}\frac{S}{N_k}\Sigma_{nk}\left(-ev_{nk}^{\alpha}.f_{nk}^{1}\right) \quad (25)$$

where α and β are the cartesian directions, Ω is the volume of unit cell and S is the spin degeneracy. Finally, the mobility tensor μ_{nk}can be calculated as

$$\mu_{nk} = \frac{\sigma_{nk}}{en_c} \quad (26)$$

where $\sigma_{nk}$is the conductivity tensor and n_c is the carrier concentration. The input parameters for the calculation of scattering rate and mobility are given in appendix.

RESULTS AND DISCUSSIONS

Electronic Structures

Pure Diborides. The density of states (DOS) was calculated for ZrB_2, CrB_2, TaB_2, TiB_2 and AlB_2 as well as for ZrB_2 containing dissolved Al, Cr and Ta using QE. The calculations utilized the linear tetrahedron method for Brillouin-zone integrations. The DOS plot as shown in Figure 12a provides an overview of the electronic structure and gives information regarding the occupied and unoccupied states as a function of energy (E). Following the normal scaling, the energy values along the x-axis were determine by subtracting the energy at the Fermi level (EF). The projected density of states (PDOS) based on the contribution of each of the elemental constituents of pure ZrB_2 is shown in Figure 12b. Overall, the results on this portion of the study confirmed the many of the characteristics on the chemical bonds within the crystal structure that have already been reported in many previous electronic structure studies [54,55]. Electrons in the s orbitals do not participate significantly in the chemical bonding, and, following the approach by Lawson et.al [54], only the role of p-orbitals of B and d-orbitals of Zr are discussed here.

From Figure 12b, significant degeneracy results in overlap of the two types of orbitals from about -13 eV up to the Fermi energy level. These overlapped peaks represent the occupied bonding states of the Zr-d and B-2p orbitals. The unoccupied peaks above the Fermi level represent the antibonding states. The unoccupied peaks above the Fermi level represent the antibonding states. As already shown by previous works [8,54], the Fermi level resides in a large pseudo-gap, which indicates the presence of strong cohesive bonds. Further examination of the partial DOS shows the extent of the c-orientated inter-layer bonding between Zr and B planes from the p-d hybridization as shown in Figure 12c.

a)

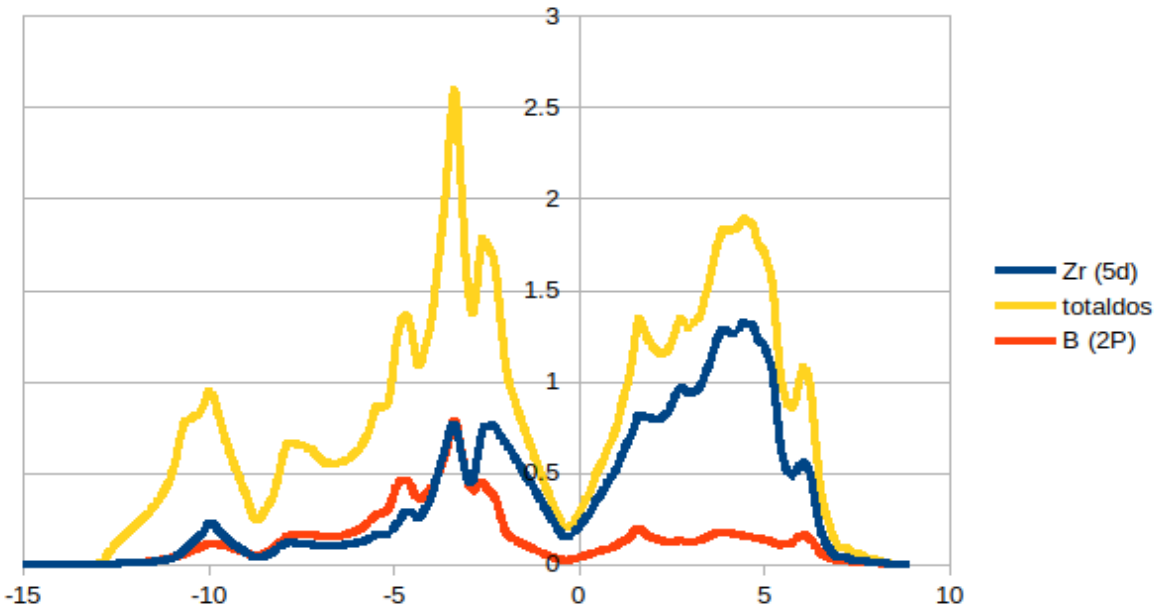
3
2.5
2
1.5
1
0.5
0
-15
-10
-5
0
5
10
Zr (5d)
totaldos
B (2P)

b)

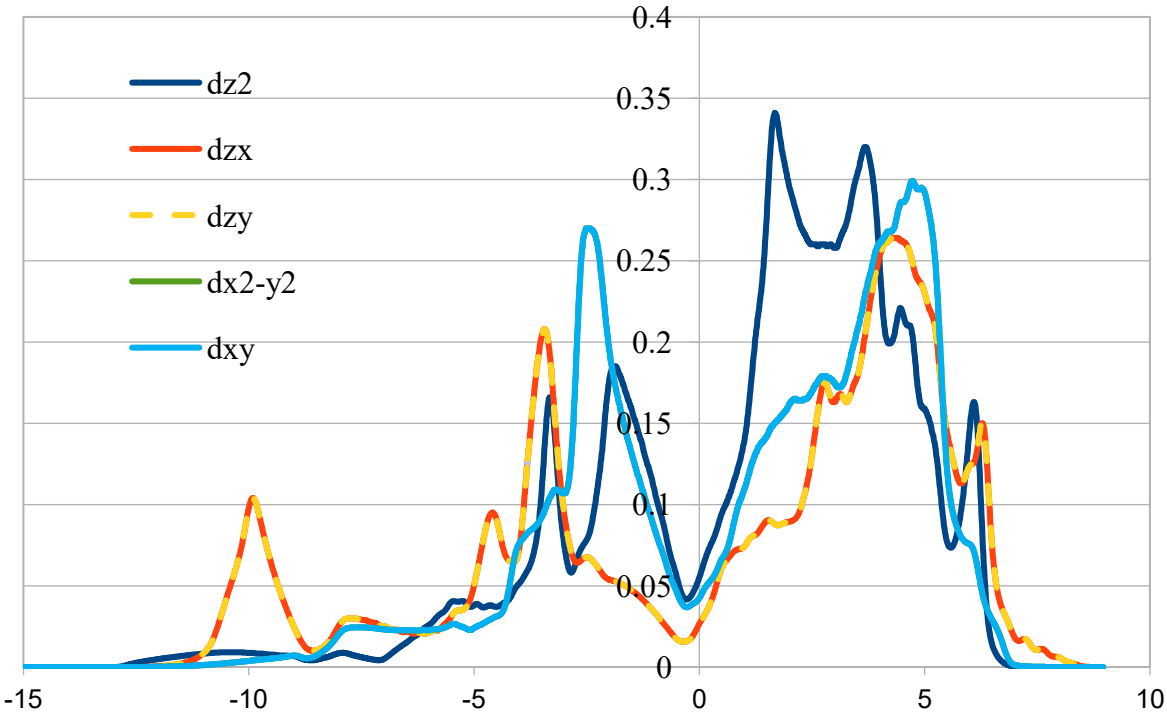
dz2
dzx
dzy
dx2-y2
dxy
0.4
0.35
0.3
0.25
0.2
0.15
0.1
0.05
0
-15
-10
-5
0
5
10

c)

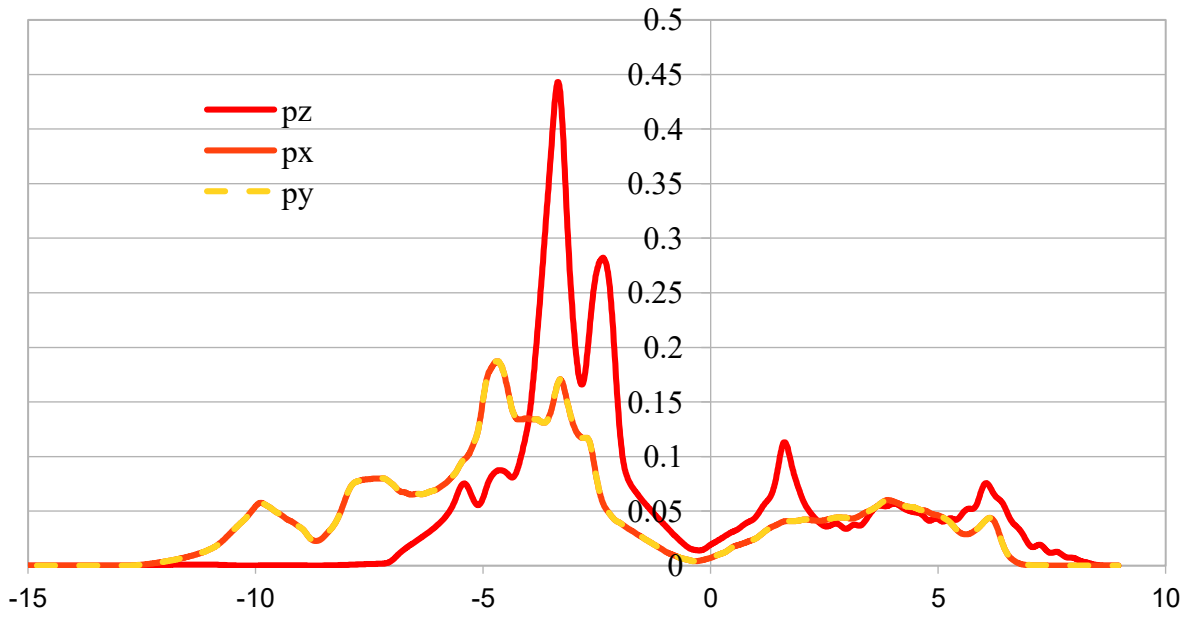

Figure 12. Plots of a) total and projected Density of States (DOS) of ZrB_2 from individual atom types and the contributions from b) the d orbitals from Zr and c) the p orbitals from B.

The energy level of the pseudo gap that coincides with the Fermi level is indicative of high electron velocities and metallic behavior, which result from the metallic bonding characteristics of the Zr-d orbitals. This, in turn, results in high thermal conductivity in these materials [54]. The partial DOS plots for TiB_2, TaB_2 and CrB_2 are shown in Figure 13. As indicated these figures, the main feature of transition metal diborides has been the consistent presence of a pseudo gap near the Fermi level [56]. The occupied states near the Fermi level for TiB_2, TaB_2 and CrB_2 are similarly dominated by the d-orbital electrons. In the case of TiB_2 shown in Figure 13a, the partial DOS from the Ti-3d and B-2p bands are energetically degenerate from the bottom of valence band to the Fermi level. This indicates strong covalent p-d hybridization and the absence of filled anti-bonding states, [57] which is like ZrB_2. For TaB_2 and CrB_2, the Fermi level is no longer near the pseudo gap as shown in Figure 13b and Figure 13c. Rather, Fermi level is at a

higher energy than the pseudo gap, which indicates partial occupancy of antibonding states due to the additional electron in the group V and VI metals compared to Ti and Zr from group IV. As has been demonstrated in previous studies [8,58,59], occupied anti-bonding states decrease the chemical stability of these phases.

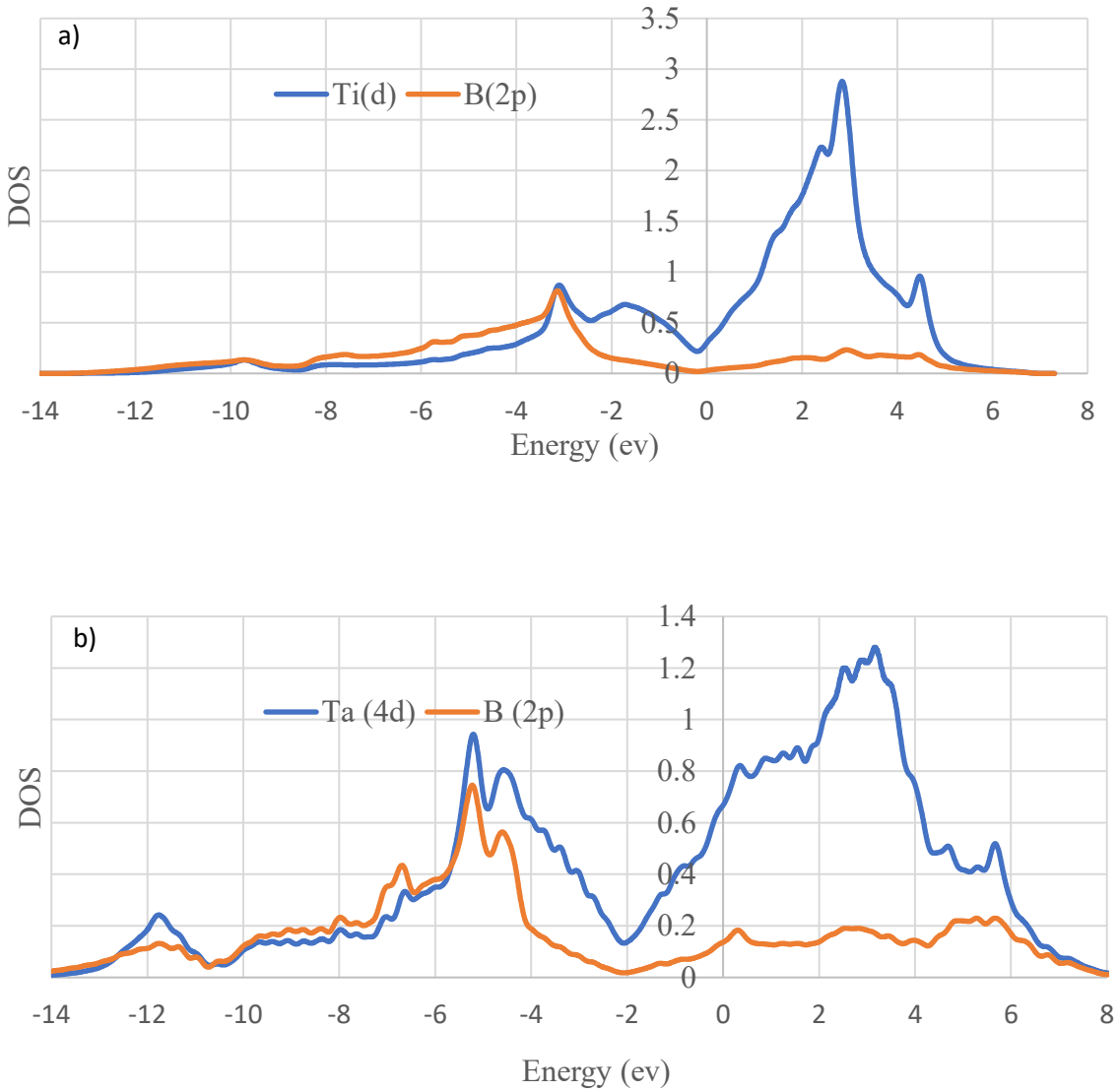

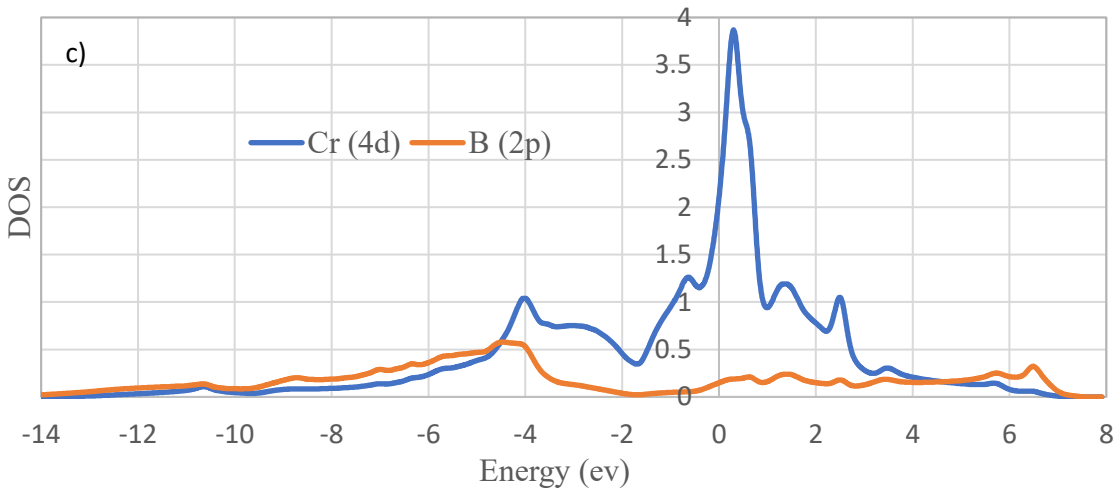

Figure 13. Projected Density of States (DOS) for B(2p) and their respective d bands (with increasing number of valence Electron) for **a)** TiB_2, **b)** TaB_2, **c)** CrB_2. The estimated energy position of the pseudo gap is marked.

Overall, the general topology of DOS for the four types of diborides shows the predominant role of the pseudo gap and the shift of the energy levels for the p and d bands in their respective DOS follows the rigid-band model for alloys [60] as shown previously [10]. The number of occupied states at the Fermi level N(EF) contributed by the d-band increases from 0.34 states/eV for TiB_2 to 0.7 states/eV for TaB_2, and to 2.2 states/eV for CrB_2, which is like results from previous theoretical studies: ~0.3 states/eV for TiB_2 [57,61], 0.75 states/eV for TaB_2 states/eV [62] and 2.5 for CrB_2 [8].

To complete the analysis on the bonding mechanism, the electronic structure of AlB_2 was re-evaluated as shown in Figure 14. The pseudo gap for AlB_2 was near the Fermi level, but, as noted from previous studies [8,63], this is not due to the p-d hybridization. Rather, it is caused by a strong planar B(p)-B(p) interaction.

As evident from Figure 15, only the x and y orientated contributions for the p-orbitals from B affect the deep pseudo gap less than 1 eV below the Fermi level. Roles of the z

component of the p-orbitals for B as well as those from the Al-Al and Al-B interactions are generally considered insignificant [8].

Doped diborides. To systematically evaluate the effect of solid solution additions on the electronic structures of the diborides, metals like Al, Cr and Ta were added to ZrB_2 at the level of 12.5 at% substitution. Figure 16 shows the DOS of ZrB_2 containing with 12.5 at% Ta in a $(Zr,Ta)B_2$ solid solution. Partially replacing Zr with Ta shifts the pseudo gap level due to the increased occupancy of the anti-bonding states mostly by Ta 5d electrons. Since this also contributes to metallic behavior, the thermal conductivity of $(Zr,Ta)B_2$ is lower than pure ZrB_2.

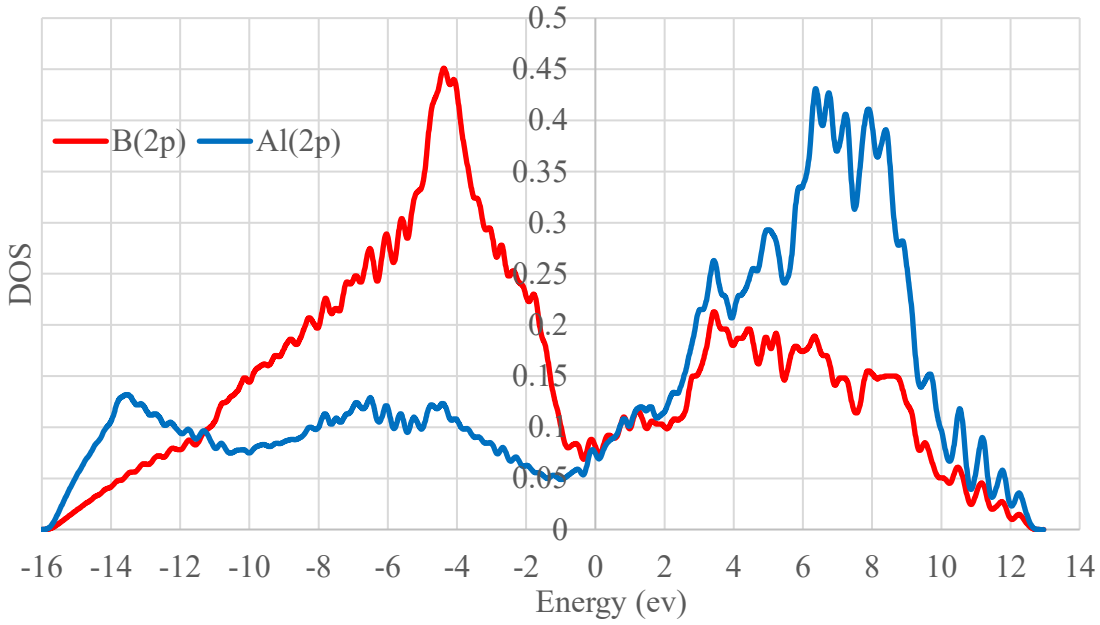

Figure 14. Partial DOS of AlB_2

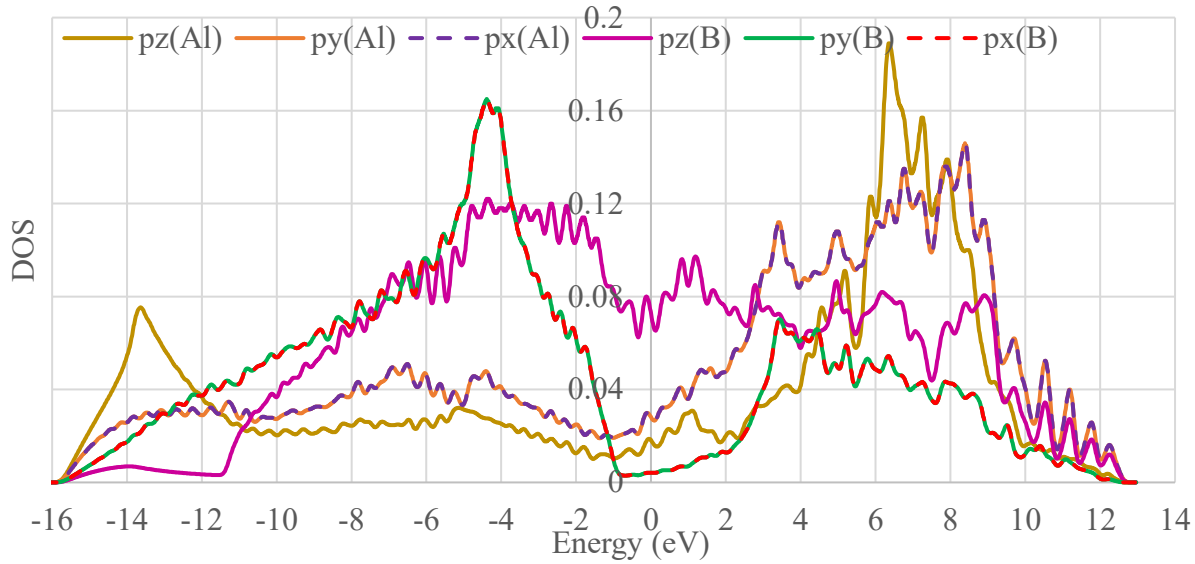

Figure 15. Partial DOS of P_x, P_y and P_z of Al and B in AlB_2

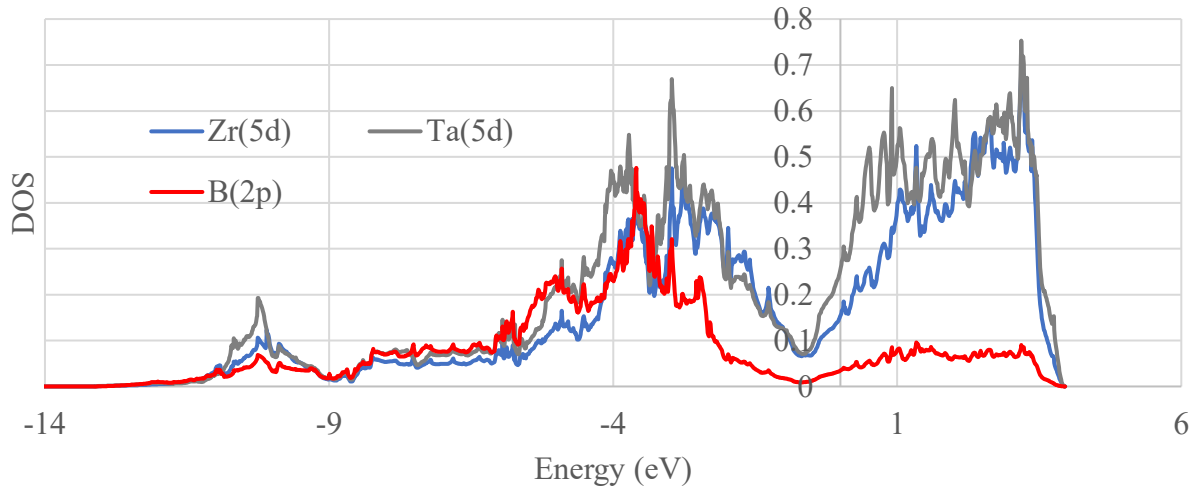

Figure 16. Plot of Partial DOS of ZrB_2 alloyed with Ta (12.5%)

Figure 17 shows the DOS of $(Zr,Cr)B_2$ revealing that the N(EF) is shifted from 0.19 states/eV for pure ZrB_2 to 1.1 states/eV for $(Zr,Cr)B_2$. Figure 18 shows the total and partial DOS for $(Zr,Al)B_2$. The pseudo gap does not change significantly, and the N(EF) values remain less than 0.2 states/eV for both Zr 5d and Al 2p orbitals. In addition, new degeneracy, and strong

interactions between Zr 5d and Al 2p were observed between 6 to 2 eV below the Fermi level, which were not present in ZrB_2. This is caused by the p-d hybridization along the close packed metal planes in the structure. In part, the directional bonding may contribute to the retention of the pseudo-gap characteristics and low N(EF) near the Fermi level.

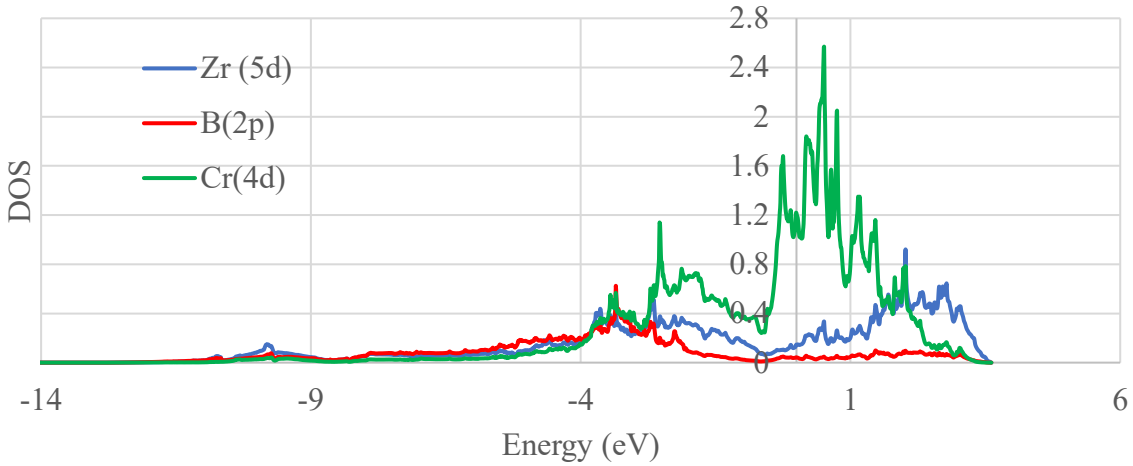

Figure 17. Plot of Partial DOS of ZrB_2 doped with Cr (12.5%)

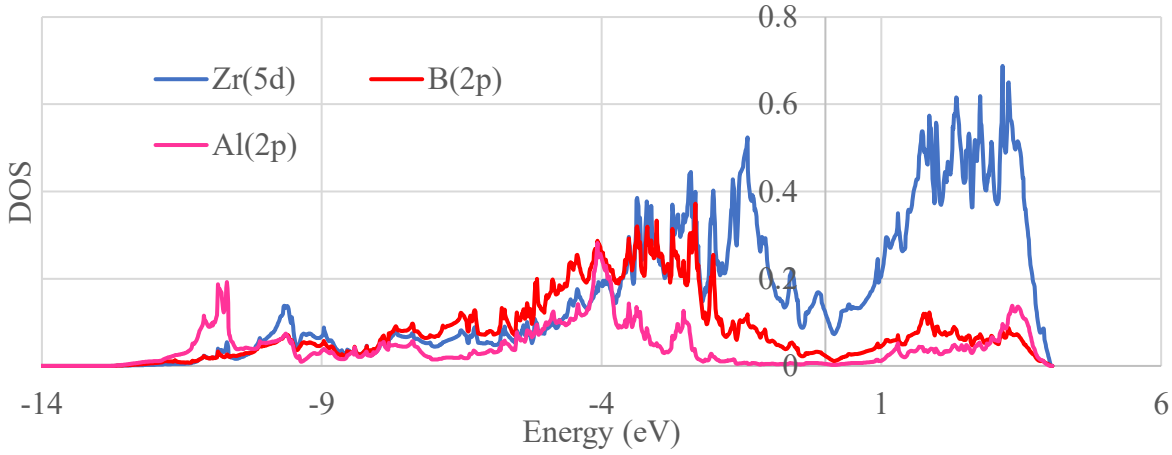

Figure 18. Plot of Partial DOS of ZrB_2 doped with Al (12.5%)

Resistivity

The EPW code [43] was used to measure the resistivity of all diborides, including the electron-phonon interactions. For electronic minimization, a convergence threshold of 10^9 eV was used, and for geometric optimization, a threshold of 10^4 eV/ was used. For both estimates, the cut-off energy was set to 45 Ry, and a first order Marzari-Vanderbilt-DeVita-Payne cold smearing with a diameter of 0.2 eV was used.

Figure 19 shows the band structure of pure ZrB_2 along with wannier interpolation along G-M-K-G-A-L. And Figure 20 shows the predicted resistivity of pure ZrB_2 from present study with previous experimental [6,13] and theoretical works [10]. Experimental measurements of electrical resistivity of ZrB_2 found a value of 7.3 μΩ cm at 300K [6], which is close to the value of 7.74 μΩ cm from the present study. The electron collides only because the lattice is not completely normal, according to our findings. The variations from an ideal lattice are divided into two categories.

a) Thermal excitation of the ions causes lattice vibrations (phonons) of the ions around their equilibrium position.

b) Any and all static flaws, such as impurities or crystal flaws.

Since the oscillation amplitudes are too small at low T, phonon scattering is negligible, and resistivity is mostly due to static imperfections. As the temperature rises, the amplitude of lattice vibration rises, scattering more electrons and increasing resistivity. Electron-electron interactions, size effects, and scattering by impurities give rise to low temperature resistivity whereas at higher temperatures, the effects of anharmonicity become dominant. Similarly, Figure 21 shows the electronic bandstructure of TiB_2 along G-M-K-G-A-L from QE with band structure from wannier interpolation.

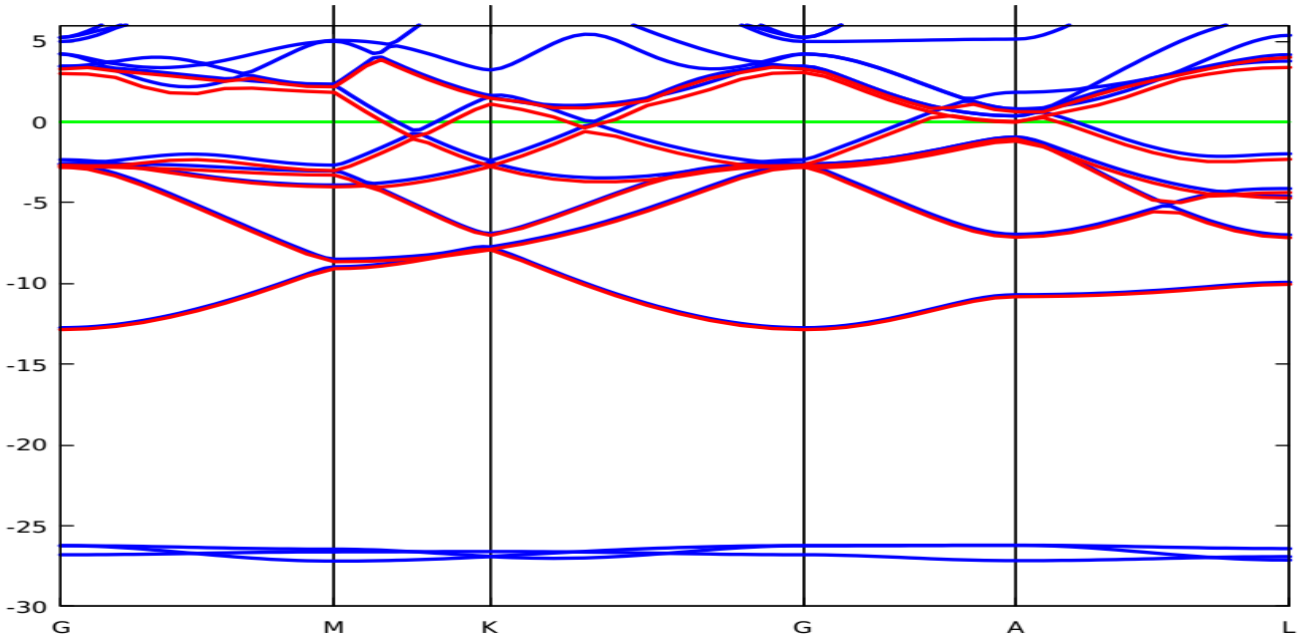

Figure 19. Band structure of ZrB_2 along G-M-K-G-A-L from DFT calculation (Blue) and via wannier interpolation (red).

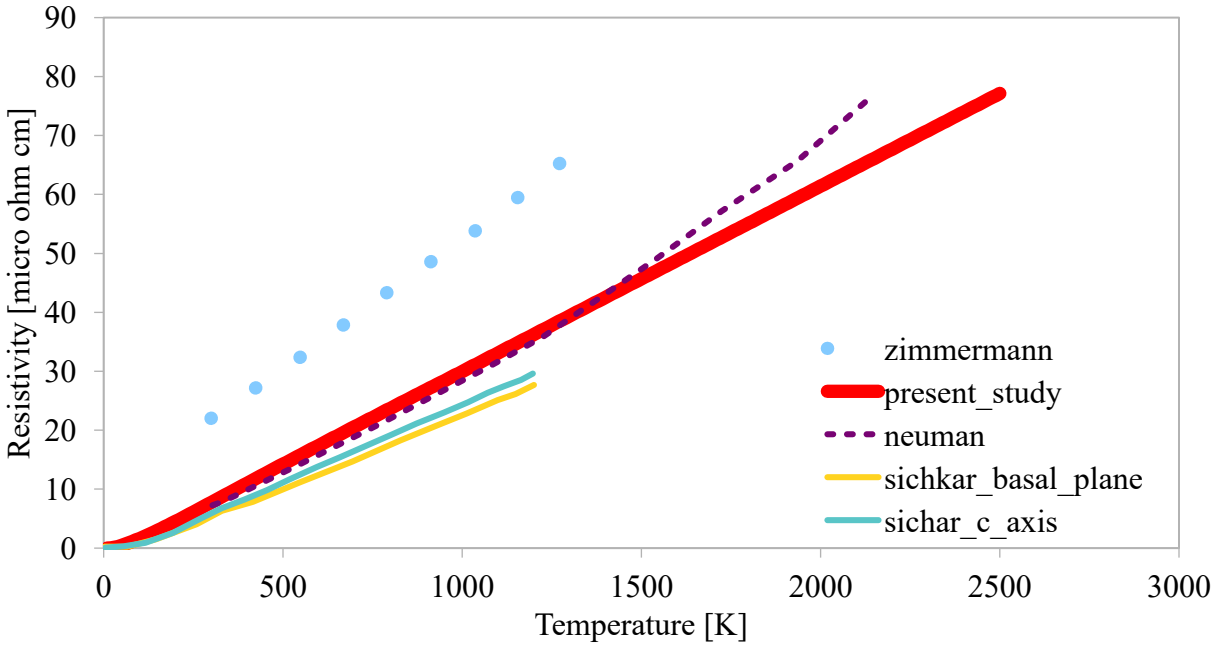

Figure 20. Resistivity of pure ZrB_2. Dotted and continuous lines denote experimental and computational woks, respectively.

Figure 22 shows electrical resistivity for TiB_2 from current study with experimental [64,65] and computational [10] works.

Similarly, Figure 23 shows electronic band structure along with wannier interpolation of CrB_2, TaB_2 and AlB_2 respectively. Finally, in Figure 24, the electrical resistivities of CrB_2, TaB_2, and AlB_2 are plotted with experimental values for CrB_2 from a previous study [66].

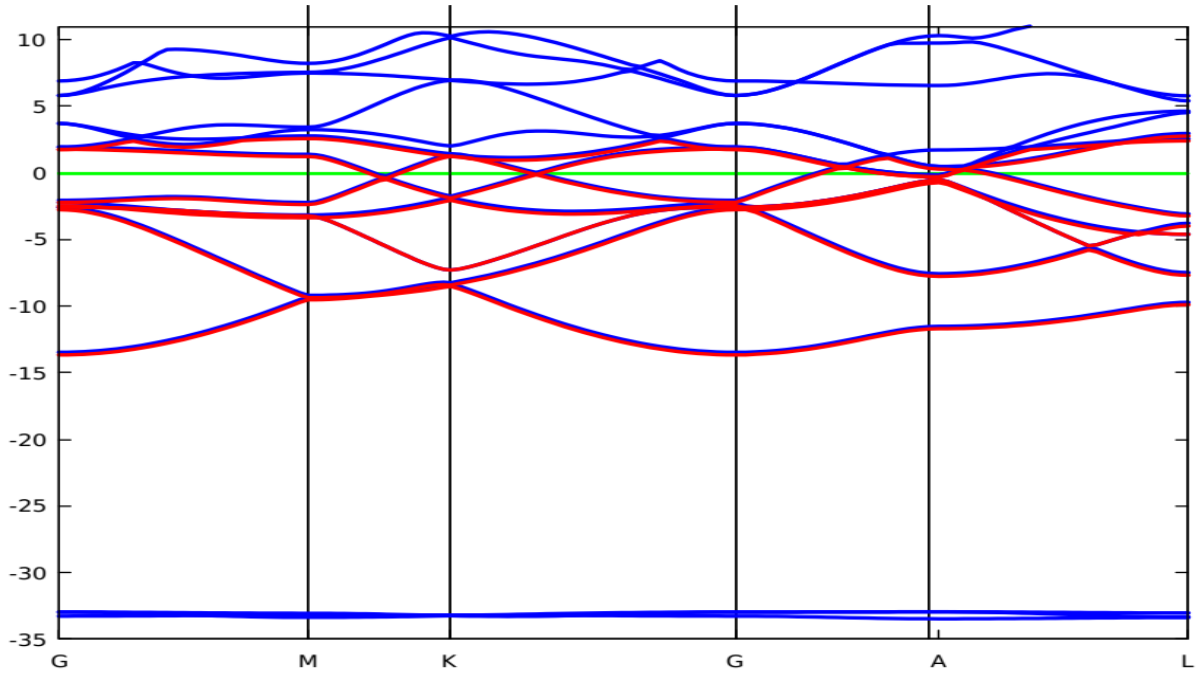

Figure 21. Band structure of TiB_2 along G-M-K-G-A-L from DFT calculation (Blue) and via wannier interpolation (red).

The resistivity is given by,

$$\rho(T) = \rho_{298} + \phi(T - 298) \quad (27)$$

Where, T is the temperature in Kelvin, ρ_{298} is the resistivity at room temperature and φ is the temperature coefficient of resistivity.

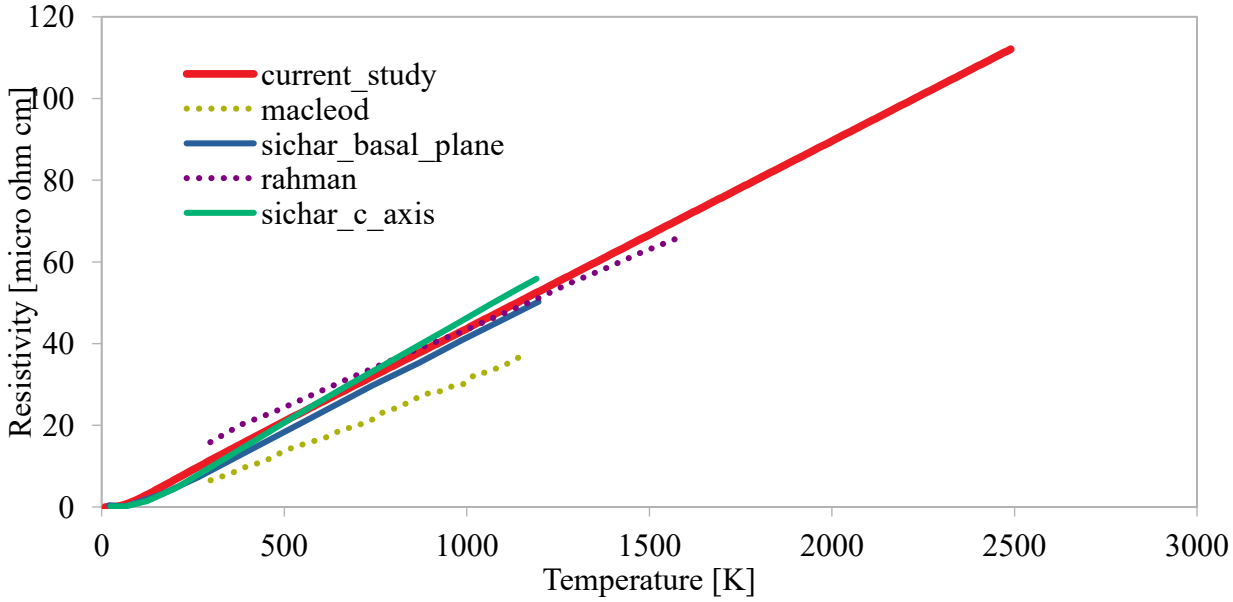

Figure 22. Resistivity of TiB_2. Dotted lines and continuous lines denote experimental and computational works, respectively.

a)

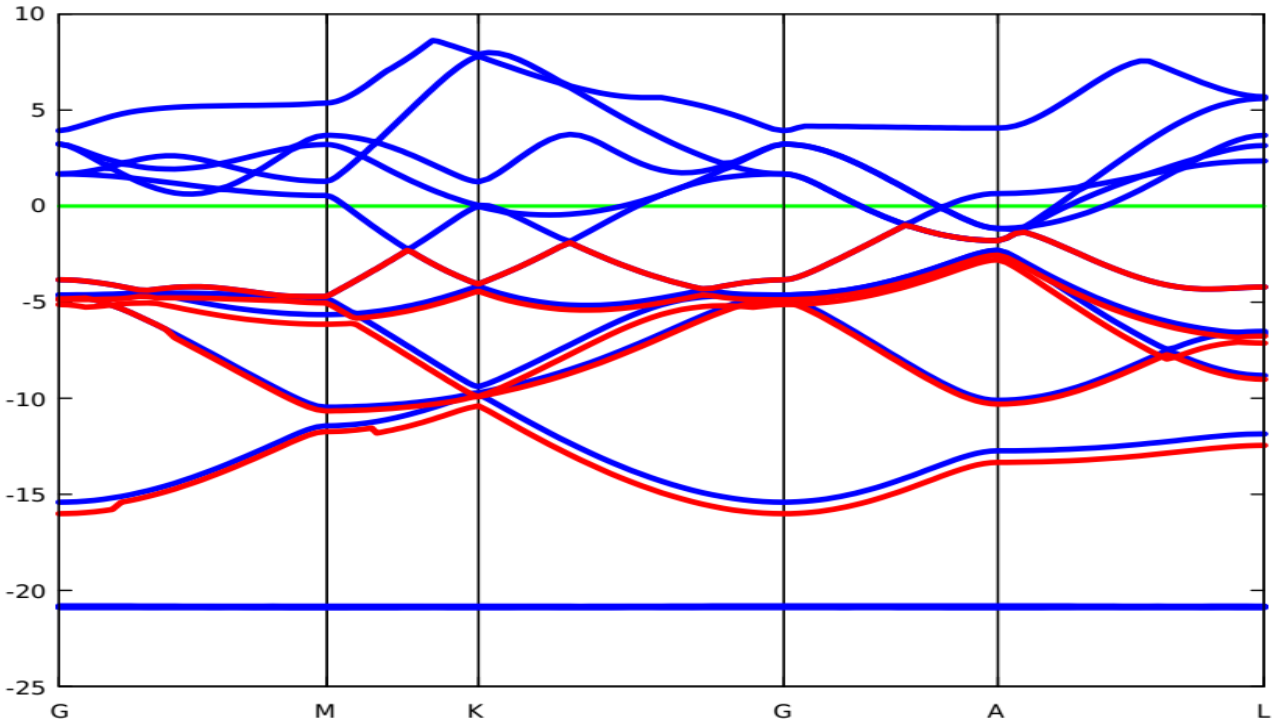

b)

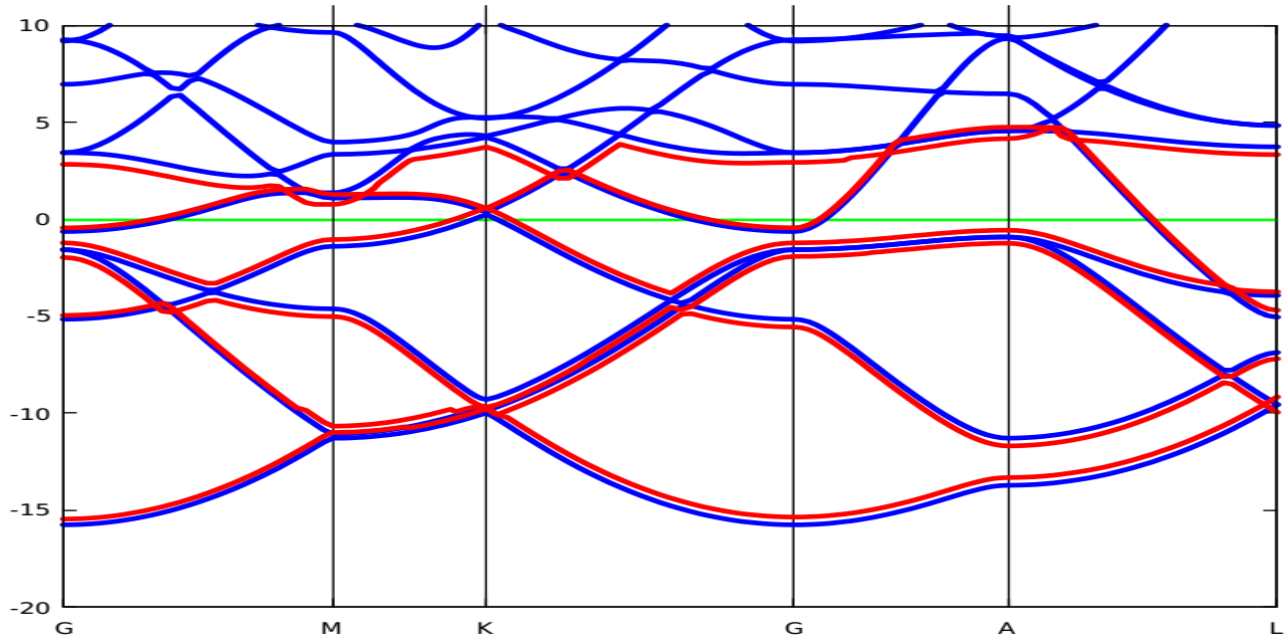

Figure 23. Electronic band structure (blue)along G-M-K-G-A-L with wannier interpolation (red) of a) CrB_2, b) AlB_2

. The ρ_{298} values of diborides from our calculations are 7.74 μΩ cm for ZrB_2, 11.53 μΩ cm for TiB_2, 4.47 μΩ cm AlB_2, 38.67 μΩ cm for TaB_2, and 57.16 μΩ cm for CrB_2.

The Matthiessen rule can be used to estimate the total electrical resistivity:

$$\rho = \rho_i + \rho_{ph} \quad (28)$$

Where ρ_i is the electrical resistivity due to scattering by impurities, which is independent of temperature, and ρ_{ph} is the resistivity due to scattering by phonons, which is temperature dependent. At extremely low temperatures, scattering of phonons is negligible because the amplitude of oscillation is exceedingly small. Thus, resistivity is small and constant. However, as temperature increases, scattering by phonons becomes more active and ρ_{ph} increases, as a result

total electrical resistivity increase. When temperature becomes large enough, (>debye temperature) scattering by phonons dominates i.e., ρ is approximately equal to ρ_{ph}.

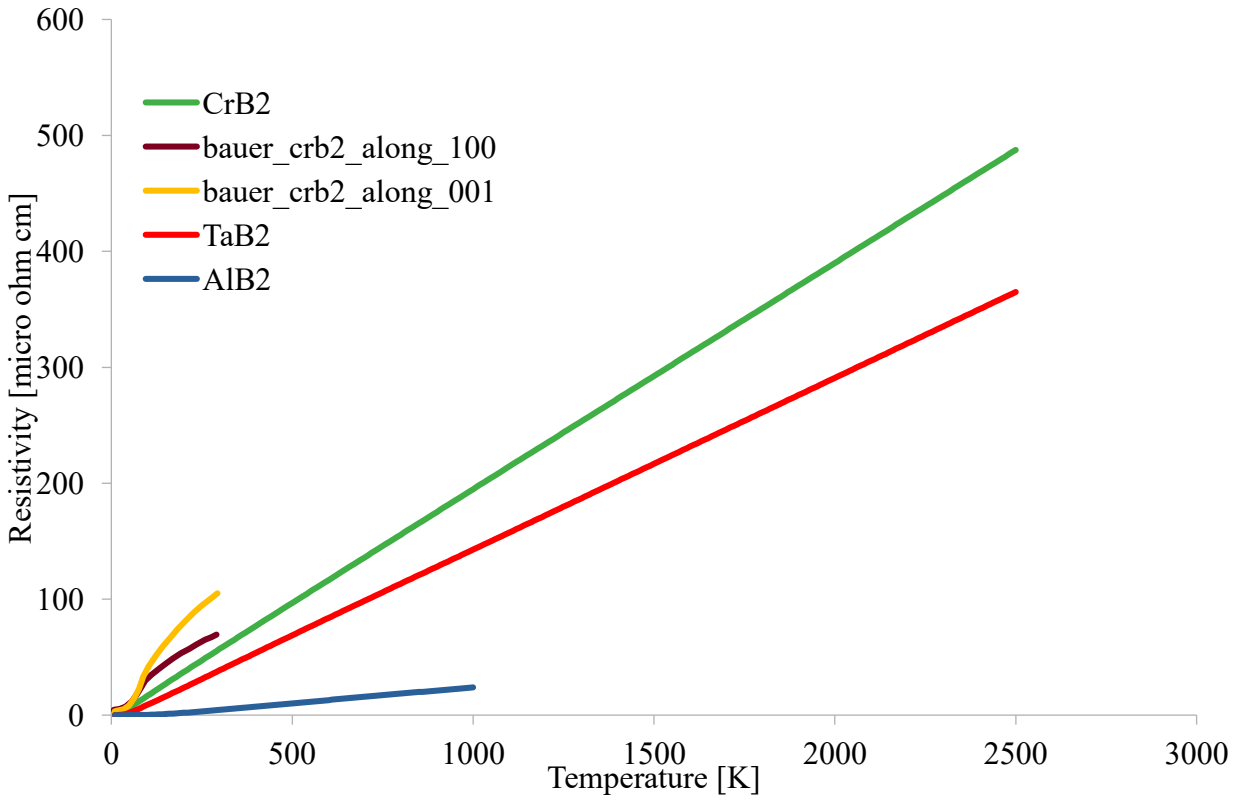

Figure 24. Resistivity of CrB_2, TaB_2 and AlB_2 along with experimental work on CrB_2.

Figure 25 compares the electrical resistivity of pure ZrB_2 and CrB_2 with ZrB_2 containing solid solution of Cr (12.5%). As expected, the resistivity of doped ZrB_2 lies in between ZrB_2 and CrB_2. Adding 12.5% Cr increases the resistivity of ZrB_2 by 2.5 times. Figure 26 shows the relaxation times of the individual diboride compounds obtained from the Boltzmann equation via EPW and BolTztrap. Comparing the relaxation times, two distinct groups of diborides are apparent, namely those with a Fermi level near the minimal gap due to either the p-d

hybridization or p-p interactions (ZrB_2, TiB_2 and AlB_2) and those with a high N(EF) due to the partial occupancy of the anti-bonding states (CrB_2 and TaB_2).

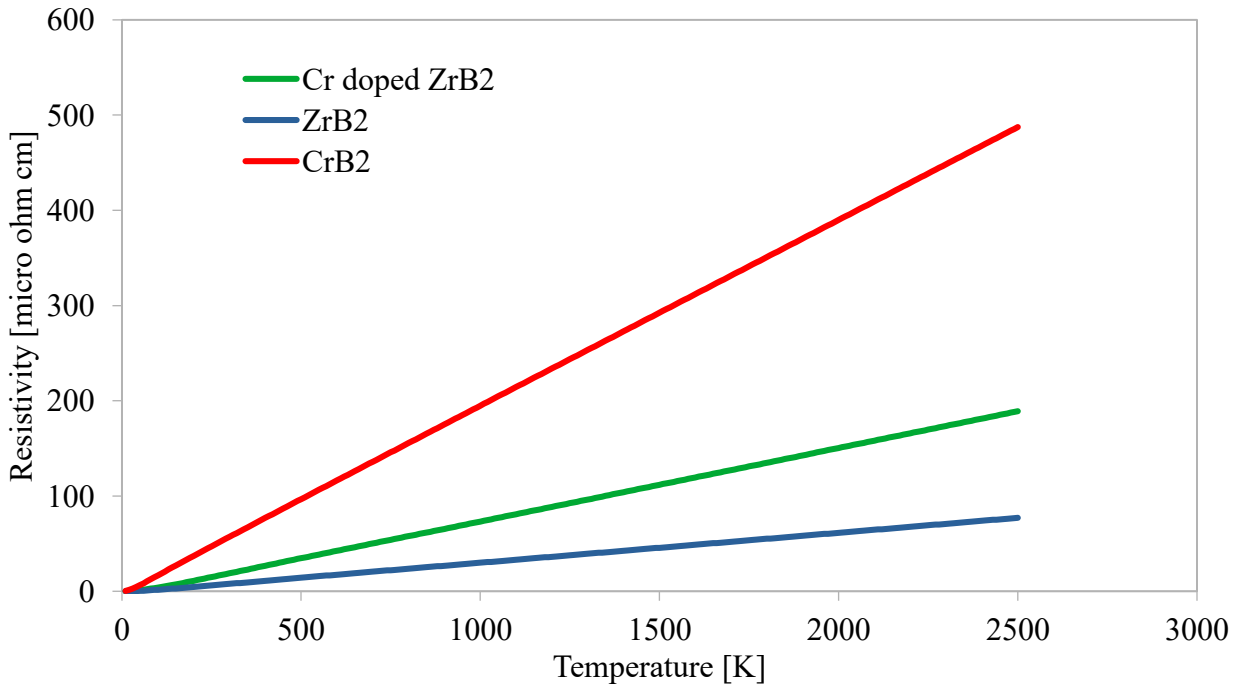

Figure 25. Variation of resistivity of pure ZrB_2, pure CrB_2 and ZrB_2 doped with Cr (12.5%) with temperature.

Thermal Conductivity.

Both phonon conduction (ph) and electron conduction(e) contribute to thermal conductivity. At low temperature, electron scattering is low due to the low frequency phonon vibrations; however, these low frequency phonons have a remarkably high mean free path which, in turn, dominates the total thermal conductivity in this temperature range. As temperature increases, the vibrational frequency of phonons increases, which results in more electron scattering and a decreased mean free path of phonons.

As a result, the electronic contribution dominates the total thermal conductivity as temperature increases. We can see from Figure 26 that there are two groups, one with a long relaxation time (ZrB_2 and TiB_2) and the other with a brief relaxation time (TaB_2, AlB_2, and CrB_2).

The relation between the electrical conductivity and electron contribution to thermal conductivity is given by Wiedemann-Franz law:

$$K_e = \sigma L_o T \tag{29}$$

Where, K_e is the electron contribution to thermal conductivity, σ is electrical conductivity, lo is the theoretical Lorenz number and T is the temperature. At a given constant temperature, we can extract the thermal conductivity from the electrical conductivity of each binary phase. But experiments [21,67] shows that the value of L is not same for all materials, so we calculate the electronic thermal conductivity by solving BTE [68].

The electronic thermal conductivity of ZrB_2, TiB_2, TaB_2 and CrB_2 is shown in Figure 27. According to Wiedemann-Franz's theorem, electronic thermal conductivity is inversely proportional to resistivity. Because of its low resistivity, ZrB_2 has a higher electronic thermal conductivity than other diborides. In comparison, unlike ZrB_2, TiB_2's relaxation time declines significantly as temperature rises.

As seen in Figure 27, the electronic conductivity suffers because of this rapid decrease in TiB_2 relaxation time. TiB_2's electronic conductivity increases at first, then stays stable, and gradually decreases. The calculated lattice thermal conductivity for all diborides is shown in Figure 28 which shows an opposite trend, indicating exponential decay**.** CrB_2 (8.12 W/mK) and TaB_2 (17.7 W/mK) had the lowest values of K_{ph} whereas those from ZrB_2 (70 W/mK) and TiB_2(64.9 W/mK) were higher.

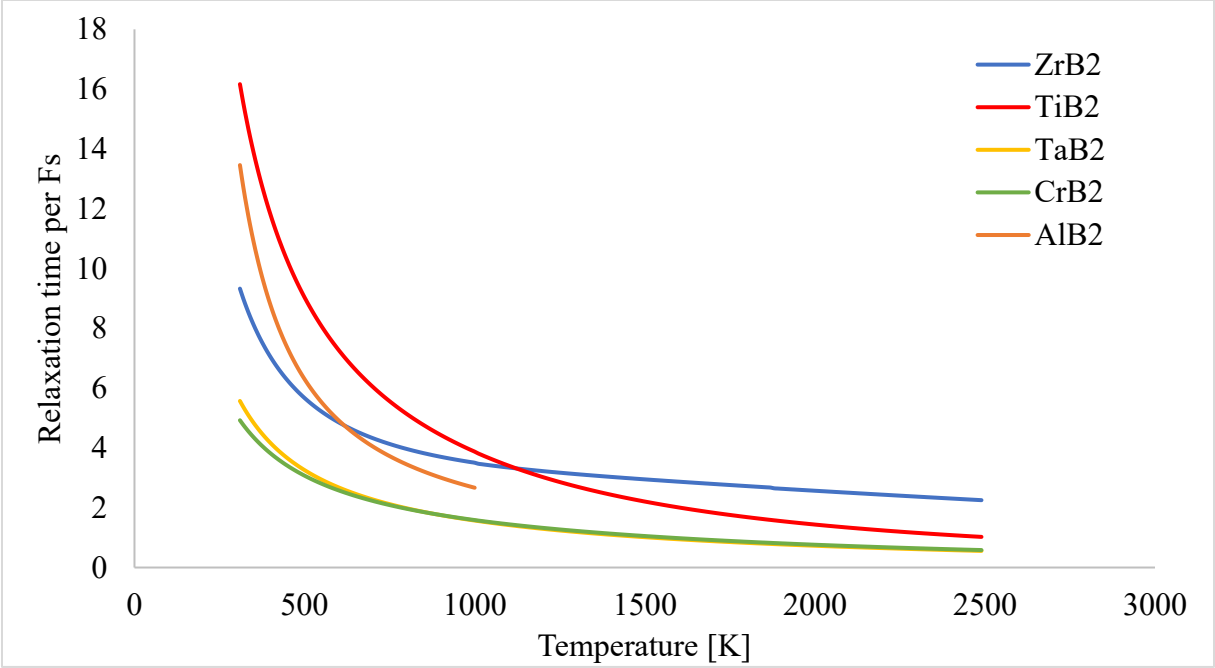

Figure 26. Relaxation time [Fs] of different metal diborides.

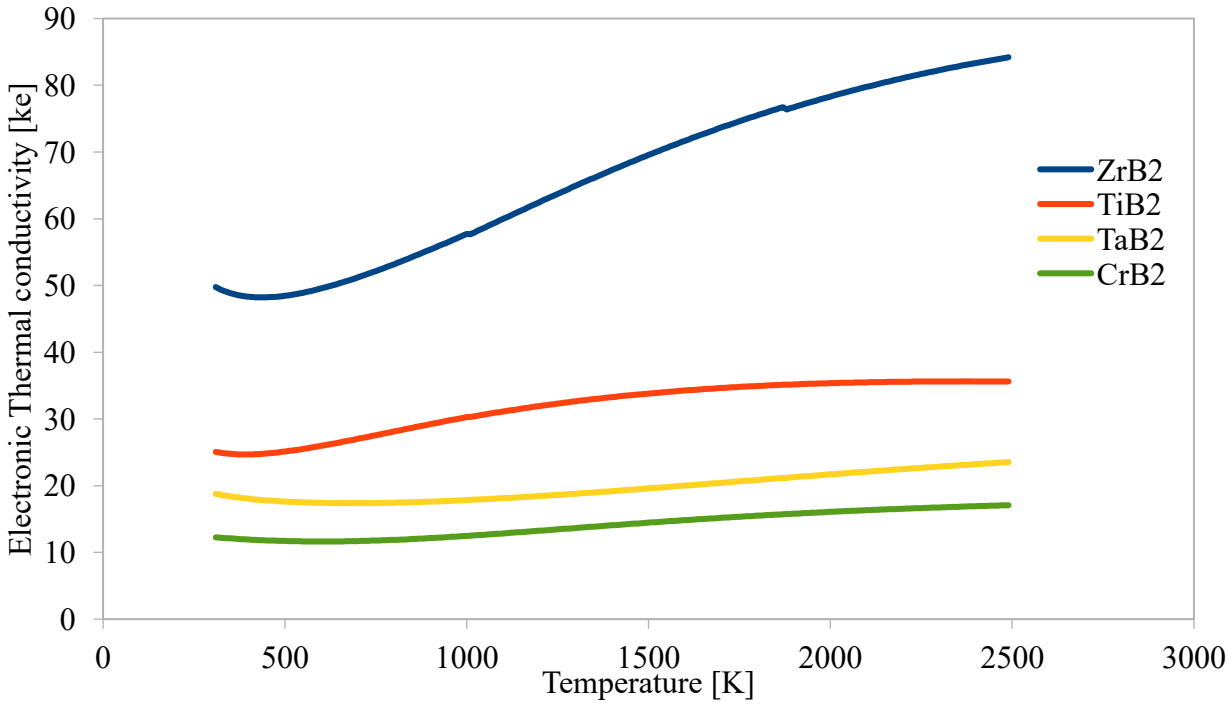

Figure 27. Variation of Electronic thermal conductivity of ZrB_2, TiB_2, TaB_2 and CrB_2 with temperature.

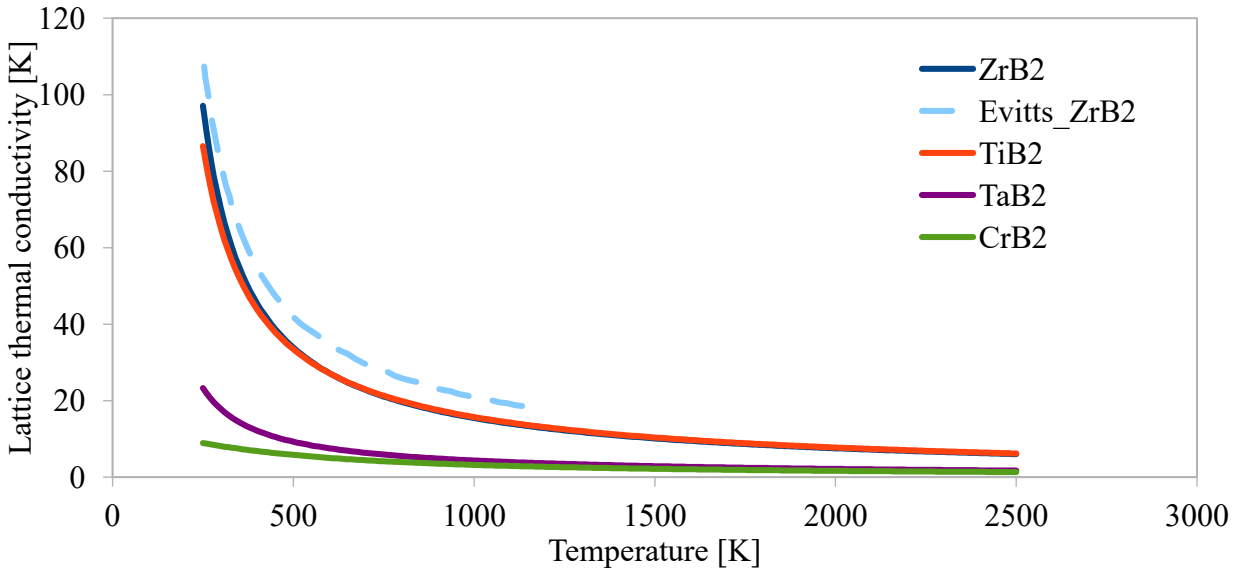

Figure 28. Lattice thermal conductivity of ZrB_2, TiB_2, TaB_2 and CrB_2 with previous work (69) of ZrB_2.

Compared the two plots, one can see that the main reason as to why ZrB_2 would stand out due to the initial and subsequent rapid rise in its electronic contribution despite the dramatic drop of its lattice contribution.

In contrast, the diboride with an already lower Ke does not generate an appreciable rise in its electronic contribution. Thus, despite a modest decrease in its lattice contribution, the total thermal conductivity of CrB_2 remains low at all temperatures. The total thermal conductivity is obtained by adding the electronic and lattice thermal conductivity, which is shown in Figure 29. Figure 29 shows that each phase has a minimum level of total thermal conductivity. This minimum point marks the transition from the the temperature regime in which the electron contribution is the dominant effect to the temperature regime where the lattice contribution to total thermal conductivity is significant. The minimum is noticeably different for different diborides owing to the variations in both contributions. Diborides with lower electrical

conductivity such as CrB_2 and TaB_2 have a lower electronic contribution. In contrast, the electron contribution for ZrB_2 and TiB_2 is higher at elevated temperature.

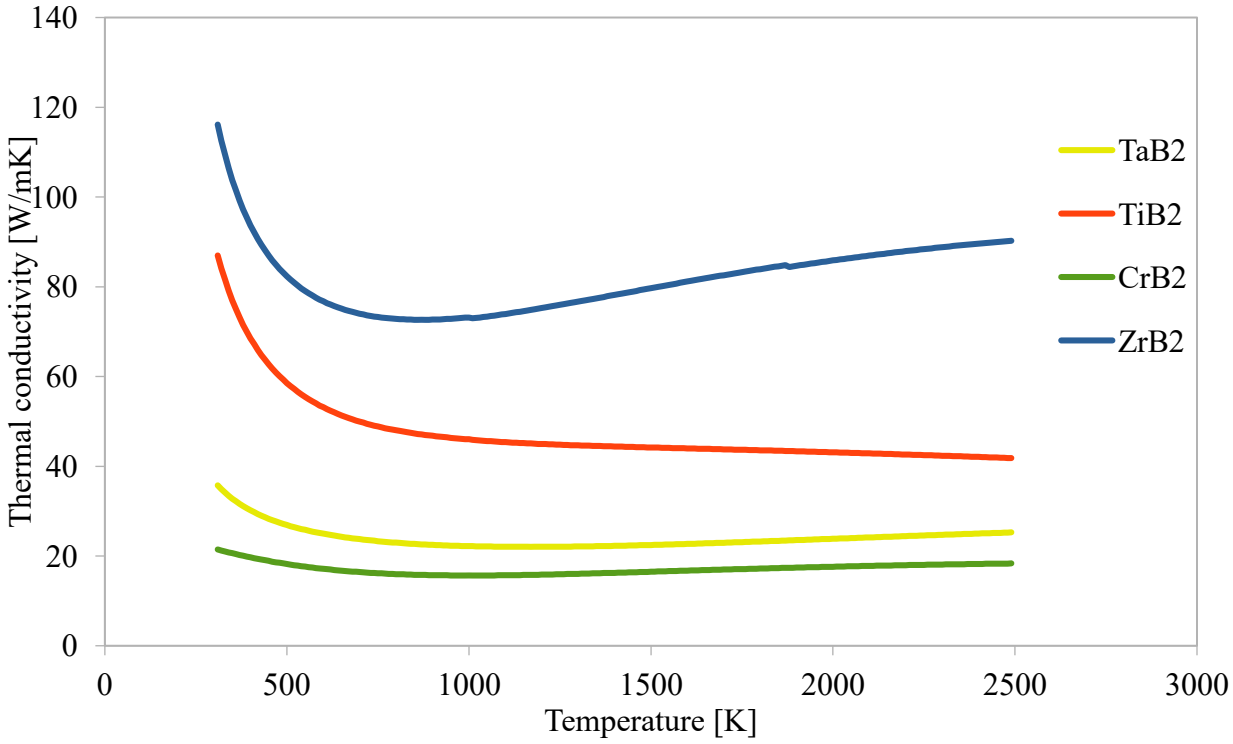

Figure 29. Total thermal conductivity of TaB_2, TiB_2, ZrB_2 and CrB_2.

Figure 30 shows AlB_2 exhibits a much more gradual decline in reaching the minimum thermal conductivity than the other diborides. This slow decline in the thermal conductivity of AlB_2 is also reported by [70]. Consequently, as shown in Figure 30, AlB_2 possesses a relatively constant level of K_e over an extended range of temperatures**.** Despite the high contribution of K_{ph} in AlB_2, the total thermal conductivity of both TiB_2 and ZrB_2 were higher than AlB_2 due to the lower K_e for AlB_2 and the lack of increasing electron contribution with increasing temperature. Figure 31 shows the comparison of our study of ZrB2 with previous study [6,13,69].

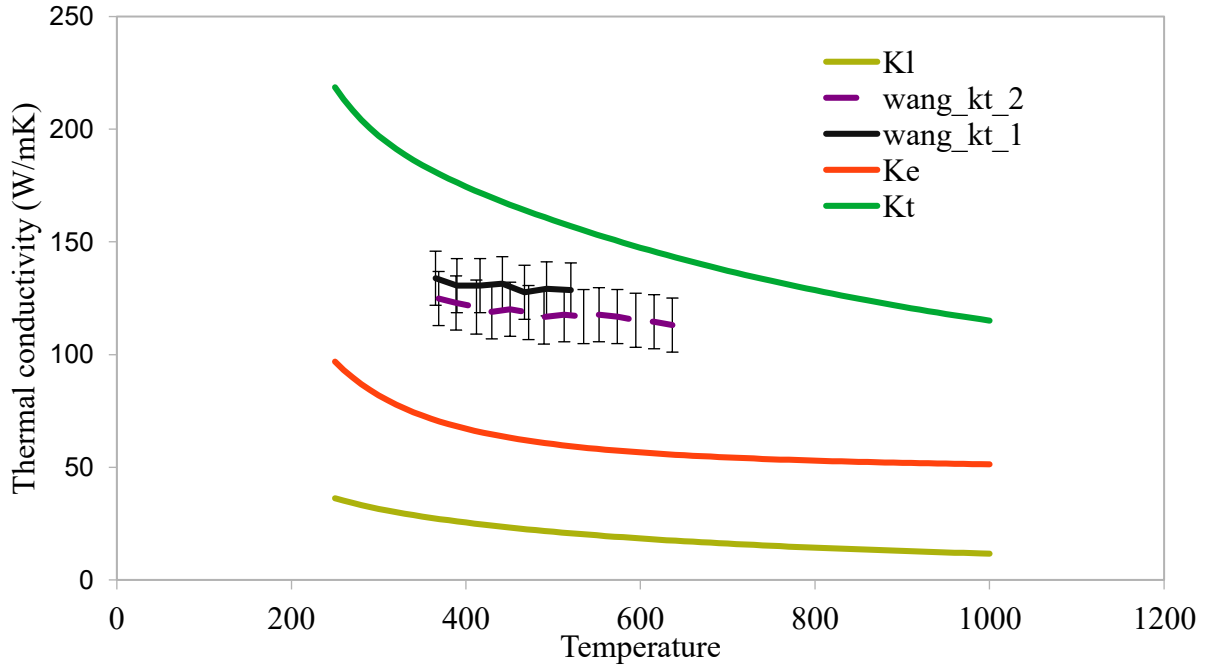

Figure 30. Variation of thermal conductivity (kt), electronic thermal conductivity (ke) and lattice thermal conductivity of AlB_2 with experimental works [70].

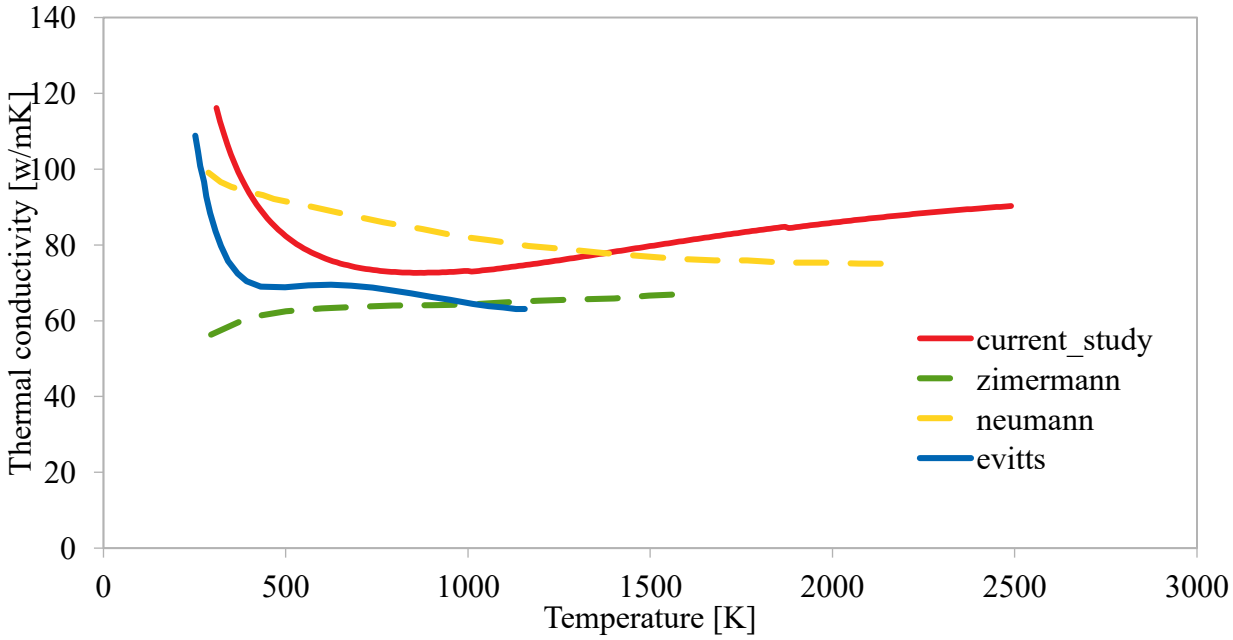

Figure 31. Variation of thermal conductivity of ZrB_2 with experimental [6,13] and computational [69] works with temperature.

The analysis was extended toward Cr-doped ZrB_2 as a model system to assess the effect of alloying toward the thermal conductivity of diborides. The analysis initially used the assumption of a linear superposition based of the Matthiessen rule which yields the relaxation time to be averaged proportionally from the binaries to estimate the scattering events in a solid solution system. We calculate the electrical resistivity of ZrB_2 comprising solid solutions of Ta and Cr atoms (each 12.5 percent) using the Matthiessen law.

The electronic thermal conductivity of each doped ZrB_2 is determined using the approximate resistivity. The electronic contribution to thermal conductivity of doped ZrB_2 with Ta and Cr is seen in Figure 32. Doping Cr on pure ZrB_2 has a higher effect than Ta, according to our calculations, owing to the high electrical resistivity of pure CrB_2.

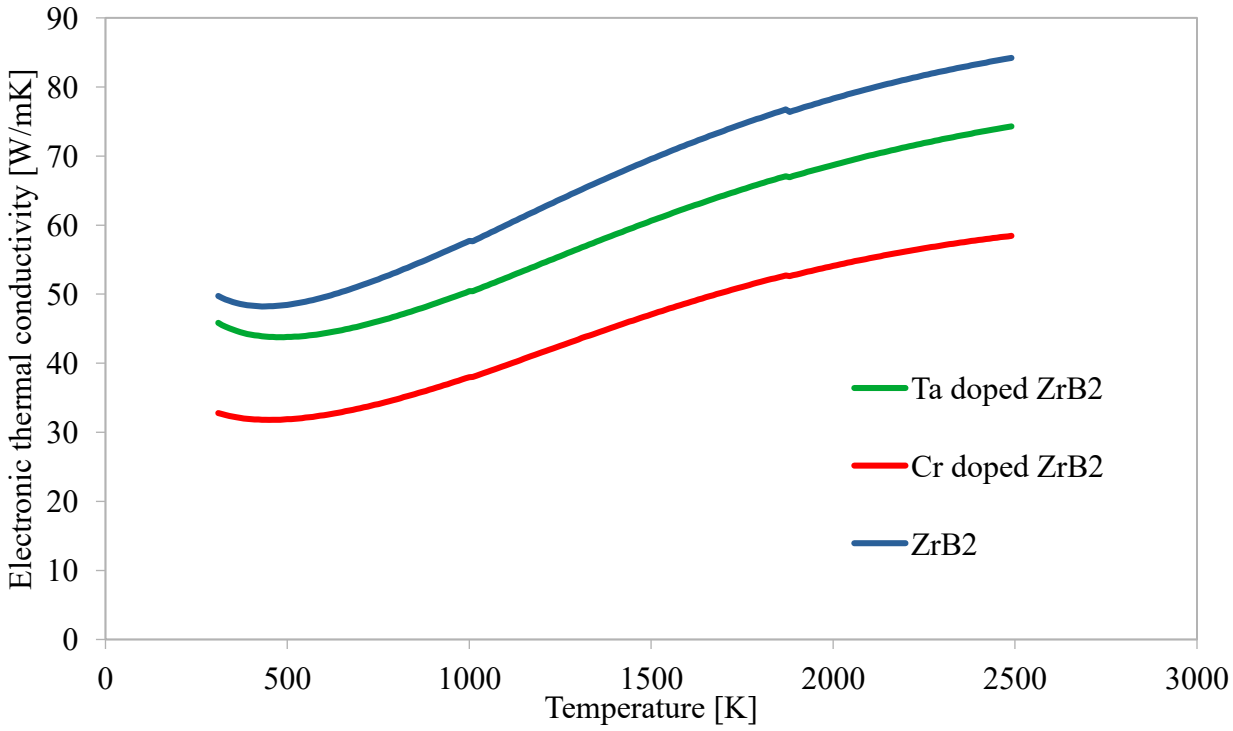

Figure 32. Variation of electronic thermal conductivity of ZrB_2 doped with Ta and Cr with temperature.

As a comparison, an additional calculation of an alloyed system was performed using a supercell that contains the Cr of the same amount. We found out that the 12.5% Cr would have instead resulted in a significant decrease in the electronic thermal conductivity by 22% and 55% at T=310K and T=2000K respectively, as shown in Figure 33. This collaborates to some extent the previously reported experimental result showing the non-proportional effect of alloying toward the thermal conductivity of ZrB_2 [14]. To further investigate this effect, we calculated and compare the scattering rate and the electron mobility in ZrB_2, CrB_2 and alloyed $(Zr_{0.875}Cr_{0.125})B_2$ as shown in Figure 34 and Figure 35. The results show the significant effect of Cr to the scattering rate and consequently the electron mobility.

The lattice thermal conductivity of Cr doped ZrB_2 is then calculated using the same approach as the binary phase. The lattice thermal conductivity of ZrB_2 falls by 19.8% and 27% at temperatures T=300K and T=2000K, respectively, as shown in Figure 36. The addition of impurity to the lattice distorts phonon transport, resulting in a reduction.

The total thermal conductivity of ZrB_2 doped with Cr produced by adding the electronic and lattice parts, as shown in Figure 37 clearly shows that the addition of Cr reduces thermal conductivity significantly. Overall, these results suggest that more theoretical efforts are clearly needed to fully understand the effect of alloying additives toward diborides in general. Within the context of the current research interests in high entropy driven advanced ceramics, such a theoretical modeling can be carefully useful to assess the potential impact of any additives toward the thermal transport properties.

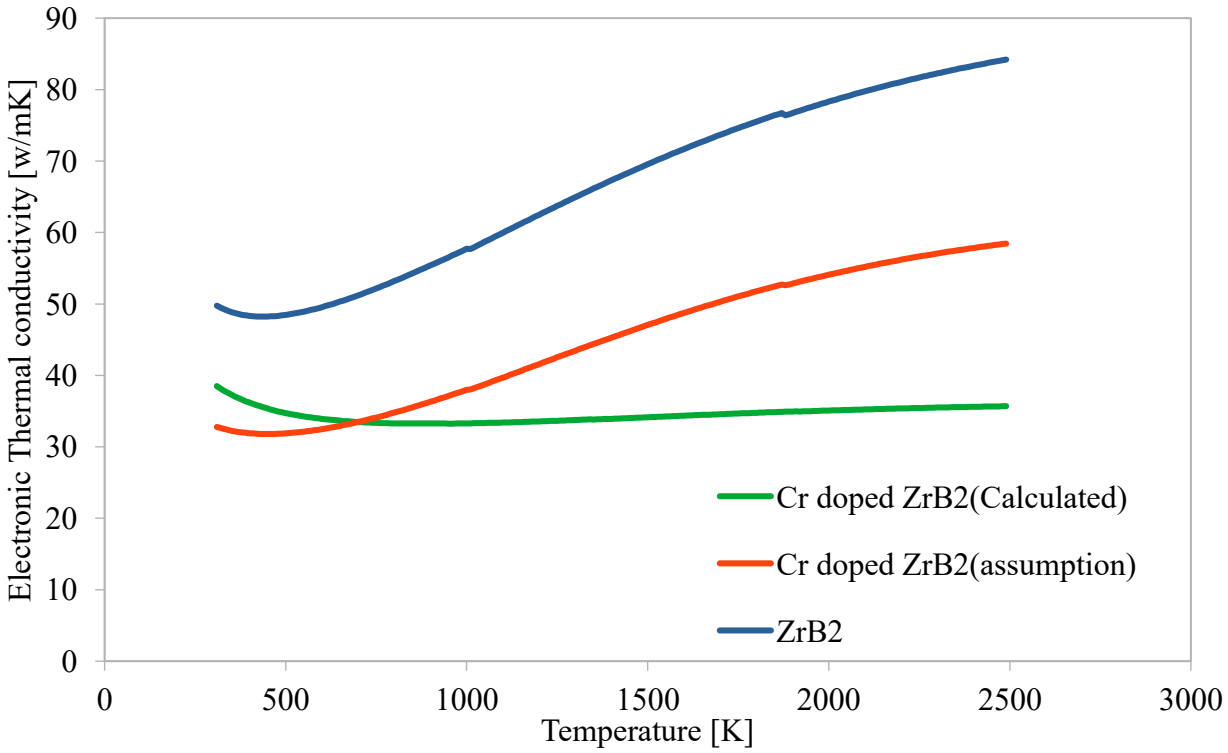

Figure 33. Comparison of electronic thermal conductivity of pure ZrB_2 with ZrB_2 doped with Cr (12.5%) [approximate (red) and calculated (green)].

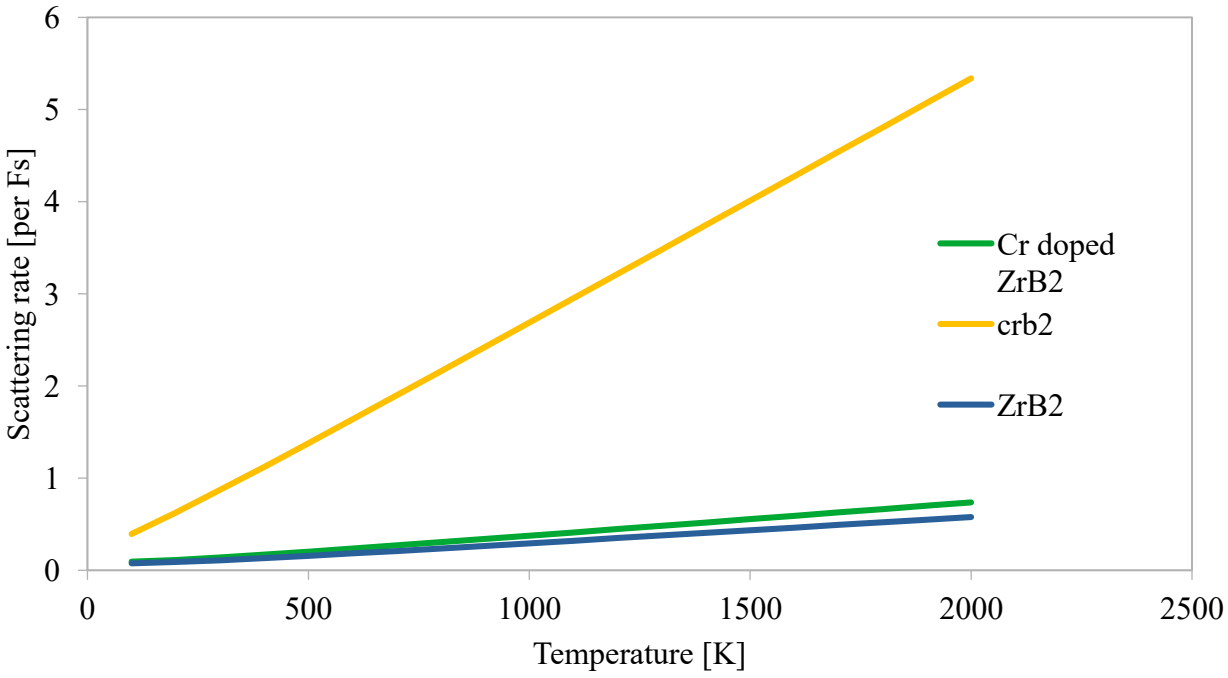

Figure 34. Scattering rate of ZrB_2, CrB_2 and Cr doped ZrB_2 (12.5%)

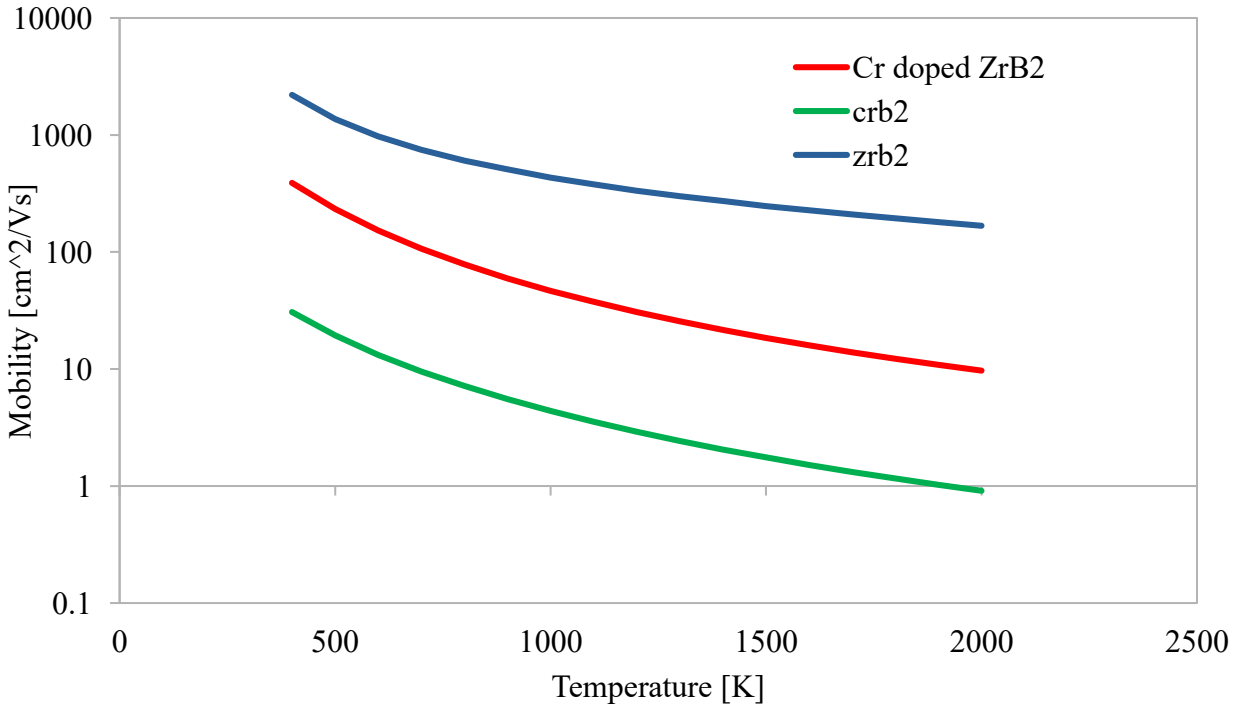

Figure 35. Mobility of ZrB_2, CrB_2 and Cr doped ZrB_2 (12.5%)

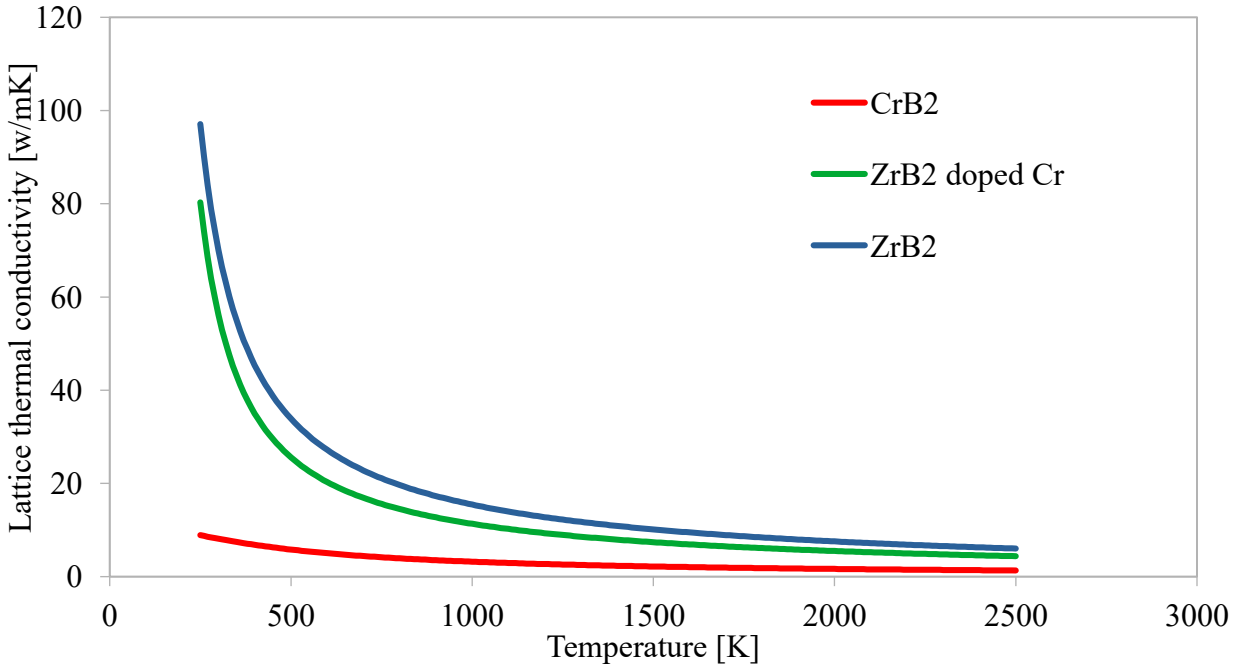

Figure 36. Lattice thermal conductivity of ZrB_2, CrB_2 and ZrB_2 doped with Cr (12.5%)

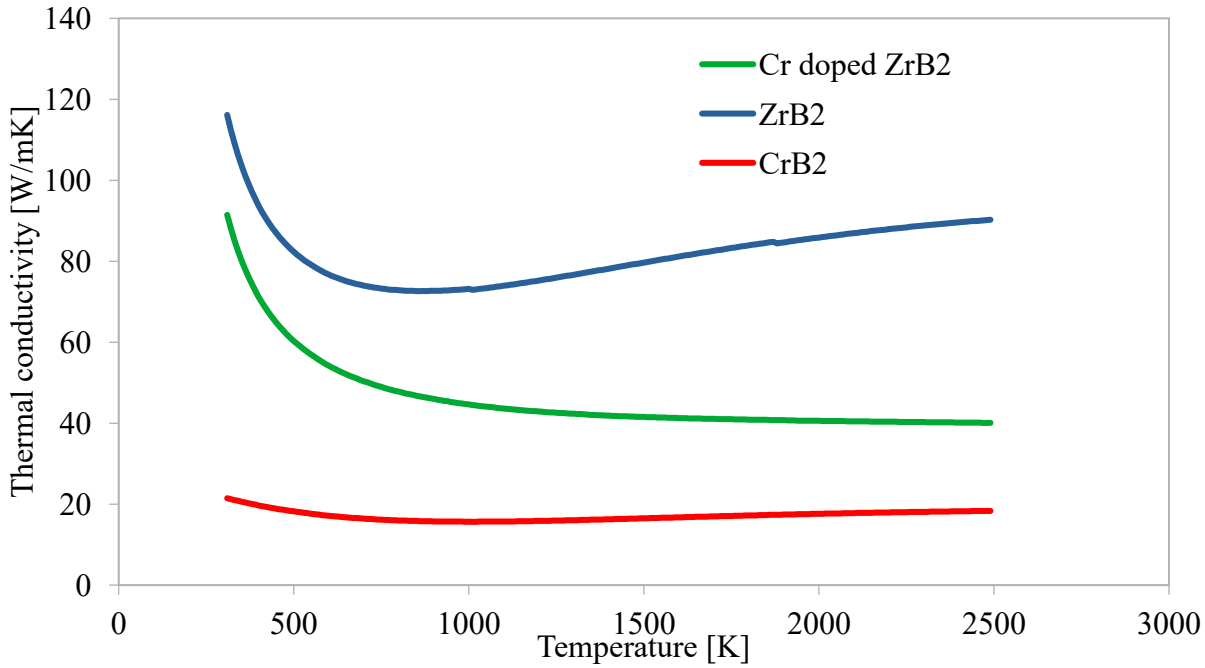

Figure 37. Total thermal conductivity of ZrB_2, CrB_2 and ZrB_2 doped with Cr (12.5%).

SUMMARY AND FUTURE WORK

The electrical structure of binary diborides as well as the influence of alloying on the density of states pure ZrB_2 have been successfully investigated. We discovered that adding transition metals like Ta and Cr to ZrB_2 causes the pseudo gap of ZrB_2 to move due to the introduction of transition metal antibonding states. In contrast to transition metal diborides, where the pseudo gap is caused by p-d hybridization, we discovered that the pseudo gap in the density of states of AlB_2 is caused by B-B interactions.

We also calculated the resistivity of various diborides, such as ZrB_2, TiB_2, TaB_2, CrB_2, and AlB_2, and discovered that ZrB_2, AlB_2, and TiB_2 have lower resistivities than CrB_2 and TaB_2, implying that ZrB_2, AlB_2, and TiB_2 have a higher electronic contribution to thermal conductivity than CrB_2 and TiB_2.

To examine the influence of alloying on the thermal conductivity of diborides, we extended our research to Cr-doped ZrB_2 as a model system. We began by assuming a linear superposition based on the Matthiessen rule, which requires the relaxation time to be averaged proportionately from the binary to predict scattering events in a solid solution system. The electron contribution to thermal conductivity with the anticipated relaxation time based on a hypothetical example of $(Zr,Cr)B_2$ may be approximated using this simplified model. The thermal conductivity of alloyed ZrB_2 would thus drop proportionately owing to the Cr addition for a certain degree of substitution (e.g., 12.5 at percent). Additionally, another computation of an alloyed system was conducted using a supercell with the same quantity of Cr as a comparison. At T=310K and T=2000K, the 12.5 percent Cr would have resulted in a substantial drop in electronic thermal conductivity of 22 percent and 55 percent, respectively. This implies that in

the diboride system, a simple additive rule to account for the electrical contribution of the alloying elements cannot be used directly and thus a careful theoretical modeling of the thermal transport property can be used useful to select and design an alloyed system for the future.

CONCLUSION

The electronic structures and the thermal conductivity were studied for a series of transition metal diborides and zirconium diboride with solid solution additions. The analysis of the electronic structures highlighted the anisotropic hybridization and orbital interactions which affect both the relative stability and the metallicity of these compounds. These characteristics in turn affects the lattice contribution at low temperature and the electron contribution at elevated temperature to the thermal conductivity. Also, the thermal properties like thermal conductivity of pure ZrB_2 is reduced by the addition of solid solutions with greater impact shown by addition of Cr. A further study in assessing the non-proportional effect of alloying toward the thermal transport property of diborides is needed.

REFERENCES

1. Lonergan J. Thermophysical properties of reaction processed zirconium diboride. Dr Diss [Internet] 2014; Available from: http://scholarsmine.mst.edu/doctoral_dissertations/2348

2. Fahrenholtz WG, Hilmas GE, Talmy IG, Zaykoski JA. Refractory diborides of zirconium and hafnium. J Am Ceram Soc 2007;90(5):1347–64.

3. Opeka MM, Talmy IG, Zaykoski JA. Oxidation-based materials selection for 2000°C + hypersonic aerosurfaces: Theoretical considerations and historical experience. J Mater Sci 2004;39(19):5887–904.

4. Chamberlain AL, Fahrenholtz WG, Hilmas GE. Low-temperature densification of zirconium diboride ceramics by reactive hot pressing. J Am Ceram Soc 2006;89(12):3638–45.

5. Shaw A. Physical properties of various conductive diborides and their binaries. Grad Theses Diss [Internet] 2015; Available from: http://lib.dr.iastate.edu/etd/14496.

6. Neuman EW, Harrington GJK, Hilmas GE, Fahrenholtz WG. Elevated temperature electrical resistivity measurements of zirconium diboride using the van der Pauw Method. J Am Ceram Soc 2019;102(12):7397–404.

7. Harrington GJK, Hilmas GE. Thermal Conductivity of ZrB_2 and HfB_2. Ultra-High Temp Ceram Mater Extrem Environ Appl 2014; 9781118700:197–235.

8. Vajeeston P, Ravindran P, Ravi C, Asokamani R. Electronic structure, bonding, and ground-state properties of AlB_2-type transition-metal diborides. Phys Rev B - Condens Matter Mater Phys 2001;63(4):1–12.

9. Post B, Glaser FW, Moskowitz D. Transition metal diborides. Acta Metall [Internet] 1954;2(1):20–5. Available from: https://www.sciencedirect.com/science/article/pii/0001616054900905.

10. Sichkar SM, Antonov VN, Antropov VP. Comparative study of the electronic structure, phonon spectra, and electron-phonon interaction of ZrB_2 and TiB_2. Phys Rev B - Condens Matter Mater Phys 2013;87(6):1–12.

11. Thompson M, Fahrenholtz WG, Hilmas G. Effect of starting particle size and oxygen content on densification of ZrB_2. J Am Ceram Soc 2011;94(2):429–35.

12. Hess K. Boltzmann Transport Equation. In: Grubin H.L, Ferry D.K, Jacoboni C editors. The physics of Submicron Semiconductor Devices [Internet]. Boston, MA: Springer US 1988;33–43. Available from: https://doi.org/10.1007/978-1-4899-2382-0_2.

13. Zimmermann JW, Hilmas GE, Fahrenholtz WG, Dinwiddie RB, Porter WD, Wang H. Thermophysical properties of ZrB_2 and ZrB_2-SiC ceramics. J Am Ceram Soc 2008;91(5):1405–11.

14. McClane DL, Fahrenholtz WG, Hilmas GE. Thermal properties of (Zr, TM) B_2 solid solutions with TM = Ta, Mo, Re, V, and Cr. J Am Ceram Soc 2014;98(2):637–44.

15. Stanfield AD, Hilmas GE, Fahrenholtz WG. Effects of Ti, Y, and Hf additions on the thermal properties of ZrB_2. J Eur Ceram Soc 2020;40(12):3824–8.

16. McClane DL, Fahrenholtz WG. Thermal properties of zirconium diboride - transition metal boride. Mater Sci Eng 2014; Masters (7265):127.

17. Taylor R. Thermal Conductivity. In: Brook RJ, editor Concise Encycl Adv Ceram Mater [Internet]. Oxford: Pergamon; 1991;472–5. Available from: https://www.sciencedirect.com/science/article/pii/B9780080347202501301.

18. Lee DW, Kingery WD. Radiation Energy Transfer and Thermal Conductivity of Ceramic Oxides. J Am Ceram Soc 1960;43(11):594–607.

19. Garai J. Physics behind the Debye temperature 2007;3(1):1–8. Available from: http://arxiv.org/abs/physics/0703001.

20. Klemens PG, Han Y-J. Umklapp Processes at Low Temperatures. In: Meissner M, Pohl RO, editors. Phonon Scattering in Condensed Matter VII. Berlin, Heidelberg: Springer Berlin Heidelberg 1993;13–4.

21. Lukas KC, Liu WS, Joshi G, Zebarjadi M, Dresselhaus MS, Ren ZF, et al. Experimental determination of the Lorenz number in Cu 0.01Bi $_2$Te $_2$.7Se 0.3 and Bi 0.88Sb 0.1$_2$. Phys Rev B - Condens Matter Mater Phys 2012;85(20):2–7.

22. Goff MM and J. Effect Mo and V lattice thermal conductivity and Lorenz number of Cr. Phys Rev B 1975;12(5):1858–67.

23. Branscomb TM, Hunter O. Improved thermal diffusivity method applied to TiB_2, ZrB_2, and HfB_2 from 200°-1300°C. J Appl Phys 1971;42(6):2309–15.

24. Zhang L, Pejaković DA, Marschall J, Gasch M. Thermal and electrical transport properties of spark plasma sintered HfB_2 and ZrB_2 ceramics. J Am Ceram Soc 2011;94(8):2562–70.

25. Samsonov G V., Kovenskaya BA, Serebryakova TI. Some physical characteristics of the diborides of transition metals of groups IV and V. Sov Phys J 1971;14(1):11–4.

26. Kurth S, Marques MAL, Gross EKU. Density-Functional Theory. In: Encyclopedia of Condensed Matter Physics [Internet]. Elsevier 2005;395–402. Available from: https://doi.org/10.1016%2Fb0-12-369401-9%2F00445-9.

27. Sholl DS, Steckel JA. Density Functional Theory: A Practical Introduction [Internet]. John Wiley & Sons, Ltd 2009. 1–235 p. Available from: https://onlinelibrary.wiley.com/doi/abs/10.1002/9780470447710.

28. Santra B, Knorr A, Scheffler M, Michaelides A. Density-Functional Theory Exchange-Correlation Functionals for Hydrogen Bonds in Water. J Chem Phys 2010;152.

29. Csonka GI, Perdew JP, Ruzsinszky A, Philipsen PHT, Lebègue S, Paier J, et al. Assessing the performance of recent density functionals for bulk solids. Phys Rev B - Condens Matter Mater Phys 2009;79(15):1–14.

30. Harl J, Schimka L, Kresse G. Assessing the quality of the random phase approximation for lattice constants and atomization energies of solids. Phys Rev B - Condens Matter Mater Phys 2010;81(11).

31. Staroverov VN, Scuseria GE, Tao J, Perdew JP. Tests of a ladder of density functionals for bulk solids and surfaces. Phys Rev B - Condens Matter Mater Phys 2004;69(7):1–11.

32. Hasnip PJ, Refson K, Probert MIJ, Yates JR, Clark SJ, Pickard CJ. Density functional theory in the solid state. Philos Trans R Soc A Math Phys Eng Sci 2014;372(2011).

33. Payne MC, Teter MP, Allan DC, Arias TA, Joannopoulos JD. Iterative minimization techniques for ab initio total-energy calculations: Molecular dynamics and conjugate gradients. Rev Mod Phys 1992;64(4):1045–97.

34. Joubert D. From ultrasoft pseudopotentials to the projector augmented-wave method. Phys Rev B - Condens Matter Mater Phys 1999;59(3):1758–75.

35. Kohn W. Analytic properties of Bloch waves and Wannier functions. Phys Rev 1959;115(4):809–21.

36. Stangel A. Wannier functions from Bloch orbitals in solids 2013;37. Available from: http://www.diva-portal.org/smash/record.jsf?pid=diva2:631027.

37. Marzari N, Souza I, Vanderbilt D. An Introduction to Maximally Localized Wannier Functions. Highlight Mon PsiK Newsl [Internet] 2003;57(3):129–68. Available from: http://www.mendeley.com/research/introduction-maximallylocalized-wannier-functions-1.

38. Wannier GH. The structure of electronic excitation levels in insulating crystals. Phys Rev. 1937;52(3):191–7.

39. Marzari N, Vanderbilt D. Maximally localized generalized Wannier functions for composite energy bands. Phys Rev B - Condens Matter Mater Phys 1997;56(20):12847–65.

40. Kresse G, Hafner J. Ab initio molecular dynamics for liquid metals. Phys Rev B 1993;47(1):558–61.

41. Kresse G, Furthmüller J. Efficiency of ab-initio total energy calculations for metals and semiconductors using a plane-wave basis set. Comput Mater Sci 1996;6(1):15–50.

42. Perdew JP, Zunger A. Self-interaction correction to density-functional approximations for many-electron systems. Phys Rev B 1981;23(10):5048–79.

43. Poncï S, Margine ER, Verdi C, Giustino F. EPW: Electron–phonon coupling, transport and superconducting properties using maximally localized Wannier functions. Comput Phys Commun [Internet] 2016; 209:116–33. Available from: http://dx.doi.org/10.1016/j.cpc.2016.07.028.

44. Madsen GKH, Singh DJ. BoltzTraP. A code for calculating band-structure dependent quantities. Comput Phys Commun 2006;175(1):67–71.

45. Siewert CE. The linearized Boltzmann equation: Concise and accurate solutions to basic flow problems. Z Angew Math Phys 2003;54(2):273–303.

46. Chaput L. Direct solution to the linearized phonon boltzmann equation. Phys Rev Lett 2013;110(26):1–5.

47. Togo A, Chaput L, Tanaka I. Distributions of phonon lifetimes in Brillouin zones. Phys Rev B - Condens Matter Mater Phys 2015;91(9).

48. Perdew JP, Burke K, Ernzerhof M. Generalized gradient approximation made simple. Phys Rev Lett 1996;77(18):3865–8.

49. Perdew JP, Burke K, Ernzerhof M. Generalized Gradient Approximation Made Simple (vol 77, pg 3865, 1996). Phys Rev Lett [Internet] 1997;78(7):1396–1396. Available from: http://www.ncbi.nlm.nih.gov/pubmed/22502509%5Cnhttp://www.ncbi.nlm.nih.gov/pubmed/10062328%5Cnhttp://link.aps.org/doi/10.1103/PhysRevLett.77.3865.

50. Blöchl PE. Projector augmented-wave method. Phys Rev B 1994;50(24):17953–79.

51. Press WH, Teukolsky SA, Vettering WT, Flannery BP. Numerical Recipes the Art of Scientific Computing Third Edition. Cambridge Univ Press 2007.

52. Zhou JJ, Park J, Lu I Te, Maliyov I, Tong X, Bernardi M. Perturbo: A software package for ab initio electron–phonon interactions, charge transport and ultrafast dynamics. Comput Phys Commun 2021;264.

53. Zhou JJ, Bernardi M. Ab initio electron mobility and polar phonon scattering in GaAs. Phys Rev B 2016;94(20):1–6.

54. Lawson JW, Bauschlicher CW, Daw MS. Ab initio computations of electronic, mechanical, and thermal properties of ZrB_2 and HfB_2. J Am Ceram Soc 2011;94(10):3494–9.

55. Rosner H, An JM, Pickett WE, Drechsler SL. Fermi surfaces of diborides: (formula presented) and (formula presented). Phys Rev B - Condens Matter Mater Phys 2002;66(2):1–6.

56. Sroba V, Fiantok T, Truchly M, Roch T, Zahoran M, Grancic B, et al. Structure evolution and mechanical properties of hard tantalum diboride films. J Vac Sci & Technol A [Internet] 2020;38(3):33408. Available from: https//doi.org/10/1116/6.0000155.

57. Yan H, Wei Q, Chang S, Guo P. A first-principal calculation of structural, mechanical, and electronic properties of titanium borides. Trans Nonferrous Met Soc China [Internet] 2011;21(7):1627-33. Available from: https://www.sciencedirect.com/science/article/pii/S1003632611609060.

58. Armstrong DR. The electronic structure of the first-row transition-metal diborides. Theor Chim Acta 1983;64(2):137–52.

59. Rosner H, Pickett WE, Drechsler SL, Handstein A, Behr G, Fuchs G, et al. Electronic structure and weak electron-phonon coupling in (formula presented). Phys Rev B - Condens Matter Mater Phys 2001;64(14):1–6.

60. Stern EA. Rigid-band model of alloys. Phys Rev 1967;157(3):544–51.

61. Kalfagiannis N, Volonakis G, Tsetseris L, Logothetidis S. Excess of boron in TiB_2 superhard thin films: A combined experimental and ab initio study. J Phys D Appl Phys 2011;44(38).

62. Zhao WJ, Wang YX. Structural, mechanical, and electronic properties of TaB_2, TaB, IrB_2, and IrB: First-principal calculations. J Solid State Chem 2009;182(10):2880–6.

63. Turner CL, Koumoulis D, Li G, Zujovic Z, Taylor RE, Kaner RB. Synthesis and characterization of aluminum diboride products using 27Al, 11B NMR and ab initio studies. J Mater Sci 2018;53(5):3309–22.

64. Mcleod AD, Haggerty JS, Sadoway DR. Electrical Resistivities of Monocrystalline and Polycrystalline TiB_2. J Am Ceram Soc 1984;67(11):705-8.

65. Rahman M, Wang CC, Chen W, Akbar SA, Mroz C. Electrical Resistivity of Titanium Diboride and Zirconium Diboride. J Am Ceram Soc 1995;78(5):1380-2.

66. Bauer A, Regnat A, Blum CGF, Gottlieb-Schönmeyer S, Pedersen B, Meven M, et al. Low-temperature properties of single-crystal CrB_2. Phys Rev B - Condens Matter Mater Phys 2014;90(6):1–15.

67. He GC, Lu H, Dong XZ, Zhang YL, Liu J, Xie CQ, et al. Electrical and thermal properties of silver nanowire fabricated on a flexible substrate by two-beam laser direct writing for designing a thermometer. RSC Adv 2018;8(44):24893–9.

68. Madsen GKH, Carrete J, Verstraete MJ. BoltzTraP2, a program for interpolating band structures and calculating semi-classical transport coefficients. Comput Phys Commun 2018; 231:140–5.

69. Evitts LJ, Middleburgh SC, Kardoulaki E, Ipatova I, Rushton MJD, Lee WE. Influence of boron isotope ratio on the thermal conductivity of uranium diboride (UB_2) and zirconium diboride (ZrB_2). J Nucl Mater [Internet] 2020;528(xxxx):151892. Available from: https://doi.org/10.1016/j.jnucmat 2019.151892.

70. Wang XJ, Mori T, Kuzmych-lanchuk I, Michiue Y, Yubuta K, Shishido T, et al Thermal conductivity of layered borides: The effect of building defects on the thermal conductivity of $TmAlB_4$ and the anisotropic thermal conductivity of AlB_2. APL Mater 2014;2(4).

APPENDIX

Structure relaxation of ZrB_2

```
&CONTROL
   calculation   = "vc-relax"
   prefix        = "ZrB2"
  outdir         = "./temp"
   pseudo_dir    = "."
   restart_mode  = "from_scratch"
/
&SYSTEM
   a                    =  3.17000e+00
   c                    =  3.54548e+00
   degauss                =  1.00000e-02
   ibrav                 = 4
   nat                   = 3
   ntyp                  = 2
   occupations             = "smearing"
   smearing               = "gaussian"
/
&ELECTRONS
   conv_thr        =  1.00000e-06
   electron_maxstep = 200
```

```
   mixing_beta      =  4.00000e-01
/
&IONS
   ion_dynamics = "damp"
/
&CELL
cell_factor = 2
cell_dynamics = 'damp-w'
cell_dofree = 'z'
/
K_POINTS {automatic}
 4  4  3  0 0 0
ATOMIC_SPECIES
Zr     91.22400  Zr.pbe-spn-kjpaw_psl.1.0.0.UPF
B      10.81100  B.pbe-n-kjpaw_psl.1.0.0.UPF
ATOMIC_POSITIONS {angstrom}
Zr      0.000000   0.000000   0.000000
B      -0.000002   1.836258   1.772742
B       1.590247   0.918128   1.772742
```

Ground state calculation of ZrB2

```
&CONTROL
   calculation   = "scf"
```

```
   prefix       = "ZrB2"
   outdir       = "./"
   pseudo_dir   = "."

/
&SYSTEM
   a                    =  3.1624766105279010
   c                    =  3.5311016001481890
   ibrav                 = 4
   nat                   = 3
   ntyp                  = 2
   occupations             = "smearing"
   degauss               = 0.02
/
&ELECTRONS
   conv_thr        =  1.0d-9
   mixing_beta     =  0.7
   mixing_mode     = 'plain'
   diagonalization  = 'david'
/
K_POINTS {automatic}
12 12  12  0 0 0
ATOMIC_SPECIES
```

Zr 91.22400 Zr.pbe-spn-kjpaw_psl.1.0.0.UPF

B 10.81100 B.pbe-n-kjpaw_psl.1.0.0.UPF

ATOMIC_POSITIONS (crystal)

Zr -0.0000000000000000 0.0000000000000000 0.0000000000000000

B 0.3333330000000032 0.6666669999999968 0.5000000000000000

B 0.6666669999999968 0.3333330000000032 0.5000000000000000

Non self consistent calculation

```
&control
   calculation='bands',
   prefix='ZrB2',
   pseudo_dir = './',
   outdir='./',
   restart_mode = 'from_scratch'
/
 &system
   ibrav = 4,
   a                   =  3.1624766105279010
   c                   =  3.5311016001481890
   nat=  3,
   ntyp = 2,
   nbnd = 16,
   occupations = 'smearing'
```

```
   degauss = 0.02
 /
 &electrons
   diagonalization = 'david'
   mixing_mode = 'plain'
   mixing_beta = 0.7
   conv_thr =  1.0d-9
 /
ATOMIC_SPECIES
Zr     91.22400  Zr.pbe-spn-kjpaw_psl.1.0.0.UPF
B      10.81100  B.pbe-n-kjpaw_psl.1.0.0.UPF
ATOMIC_POSITIONS (crystal)
Zr  -0.0000000000000000  0.0000000000000000  0.0000000000000000
B    0.3333330000000032  0.6666669999999968  0.5000000000000000
B    0.6666669999999968  0.3333330000000032  0.5000000000000000
K_POINTS crystal
216
 0.00000000  0.00000000  0.00000000  4.629630e-03
  0.00000000  0.00000000  0.16666667  4.629630e-03
  0.00000000  0.00000000  0.33333333  4.629630e-03
  0.00000000  0.00000000  0.50000000  4.629630e-03
  0.00000000  0.00000000  0.66666667  4.629630e-03
  0.00000000  0.00000000  0.83333333  4.629630e-03
```

0.00000000 0.16666667 0.00000000 4.629630e-03

0.00000000 0.16666667 0.16666667 4.629630e-03

0.00000000 0.16666667 0.33333333 4.629630e-03

0.00000000 0.16666667 0.50000000 4.629630e-03

0.00000000 0.16666667 0.66666667 4.629630e-03

0.00000000 0.16666667 0.83333333 4.629630e-03

0.00000000 0.33333333 0.00000000 4.629630e-03

0.00000000 0.33333333 0.16666667 4.629630e-03

0.00000000 0.33333333 0.33333333 4.629630e-03

0.00000000 0.33333333 0.50000000 4.629630e-03

0.00000000 0.33333333 0.66666667 4.629630e-03

0.00000000 0.33333333 0.83333333 4.629630e-03

0.00000000 0.50000000 0.00000000 4.629630e-03

0.00000000 0.50000000 0.16666667 4.629630e-03

0.00000000 0.50000000 0.33333333 4.629630e-03

0.00000000 0.50000000 0.50000000 4.629630e-03

0.00000000 0.50000000 0.66666667 4.629630e-03

0.00000000 0.50000000 0.83333333 4.629630e-03

0.00000000 0.66666667 0.00000000 4.629630e-03

0.00000000 0.66666667 0.16666667 4.629630e-03

0.00000000 0.66666667 0.33333333 4.629630e-03

0.00000000 0.66666667 0.50000000 4.629630e-03

0.00000000 0.66666667 0.66666667 4.629630e-03

0.00000000 0.66666667 0.83333333 4.629630e-03

0.00000000 0.83333333 0.00000000 4.629630e-03

0.00000000 0.83333333 0.16666667 4.629630e-03

0.00000000 0.83333333 0.33333333 4.629630e-03

0.00000000 0.83333333 0.50000000 4.629630e-03

0.00000000 0.83333333 0.66666667 4.629630e-03

0.00000000 0.83333333 0.83333333 4.629630e-03

0.16666667 0.00000000 0.00000000 4.629630e-03

0.16666667 0.00000000 0.16666667 4.629630e-03

0.16666667 0.00000000 0.33333333 4.629630e-03

0.16666667 0.00000000 0.50000000 4.629630e-03

0.16666667 0.00000000 0.66666667 4.629630e-03

0.16666667 0.00000000 0.83333333 4.629630e-03

0.16666667 0.16666667 0.00000000 4.629630e-03

0.16666667 0.16666667 0.16666667 4.629630e-03

0.16666667 0.16666667 0.33333333 4.629630e-03

0.16666667 0.16666667 0.50000000 4.629630e-03

0.16666667 0.16666667 0.66666667 4.629630e-03

0.16666667 0.16666667 0.83333333 4.629630e-03

0.16666667 0.33333333 0.00000000 4.629630e-03

0.16666667 0.33333333 0.16666667 4.629630e-03

0.16666667 0.33333333 0.33333333 4.629630e-03

0.16666667 0.33333333 0.50000000 4.629630e-03

0.16666667 0.33333333 0.66666667 4.629630e-03

0.16666667 0.33333333 0.83333333 4.629630e-03

0.16666667 0.50000000 0.00000000 4.629630e-03

0.16666667 0.50000000 0.16666667 4.629630e-03

0.16666667 0.50000000 0.33333333 4.629630e-03

0.16666667 0.50000000 0.50000000 4.629630e-03

0.16666667 0.50000000 0.66666667 4.629630e-03

0.16666667 0.50000000 0.83333333 4.629630e-03

0.16666667 0.66666667 0.00000000 4.629630e-03

0.16666667 0.66666667 0.16666667 4.629630e-03

0.16666667 0.66666667 0.33333333 4.629630e-03

0.16666667 0.66666667 0.50000000 4.629630e-03

0.16666667 0.66666667 0.66666667 4.629630e-03

0.16666667 0.66666667 0.83333333 4.629630e-03

0.16666667 0.83333333 0.00000000 4.629630e-03

0.16666667 0.83333333 0.16666667 4.629630e-03

0.16666667 0.83333333 0.33333333 4.629630e-03

0.16666667 0.83333333 0.50000000 4.629630e-03

0.16666667 0.83333333 0.66666667 4.629630e-03

0.16666667 0.83333333 0.83333333 4.629630e-03

0.33333333 0.00000000 0.00000000 4.629630e-03

0.33333333 0.00000000 0.16666667 4.629630e-03

0.33333333 0.00000000 0.33333333 4.629630e-03

0.33333333 0.00000000 0.50000000 4.629630e-03

0.33333333 0.00000000 0.66666667 4.629630e-03

0.33333333 0.00000000 0.83333333 4.629630e-03

0.33333333 0.16666667 0.00000000 4.629630e-03

0.33333333 0.16666667 0.16666667 4.629630e-03

0.33333333 0.16666667 0.33333333 4.629630e-03

0.33333333 0.16666667 0.50000000 4.629630e-03

0.33333333 0.16666667 0.66666667 4.629630e-03

0.33333333 0.16666667 0.83333333 4.629630e-03

0.33333333 0.33333333 0.00000000 4.629630e-03

0.33333333 0.33333333 0.16666667 4.629630e-03

0.33333333 0.33333333 0.33333333 4.629630e-03

0.33333333 0.33333333 0.50000000 4.629630e-03

0.33333333 0.33333333 0.66666667 4.629630e-03

0.33333333 0.33333333 0.83333333 4.629630e-03

0.33333333 0.50000000 0.00000000 4.629630e-03

0.33333333 0.50000000 0.16666667 4.629630e-03

0.33333333 0.50000000 0.33333333 4.629630e-03

0.33333333 0.50000000 0.50000000 4.629630e-03

0.33333333 0.50000000 0.66666667 4.629630e-03

0.33333333 0.50000000 0.83333333 4.629630e-03

0.33333333 0.66666667 0.00000000 4.629630e-03

0.33333333 0.66666667 0.16666667 4.629630e-03

0.33333333 0.66666667 0.33333333 4.629630e-03

0.33333333 0.66666667 0.50000000 4.629630e-03

0.33333333 0.66666667 0.66666667 4.629630e-03

0.33333333 0.66666667 0.83333333 4.629630e-03

0.33333333 0.83333333 0.00000000 4.629630e-03

0.33333333 0.83333333 0.16666667 4.629630e-03

0.33333333 0.83333333 0.33333333 4.629630e-03

0.33333333 0.83333333 0.50000000 4.629630e-03

0.33333333 0.83333333 0.66666667 4.629630e-03

0.33333333 0.83333333 0.83333333 4.629630e-03

0.50000000 0.00000000 0.00000000 4.629630e-03

0.50000000 0.00000000 0.16666667 4.629630e-03

0.50000000 0.00000000 0.33333333 4.629630e-03

0.50000000 0.00000000 0.50000000 4.629630e-03

0.50000000 0.00000000 0.66666667 4.629630e-03

0.50000000 0.00000000 0.83333333 4.629630e-03

0.50000000 0.16666667 0.00000000 4.629630e-03

0.50000000 0.16666667 0.16666667 4.629630e-03

0.50000000 0.16666667 0.33333333 4.629630e-03

0.50000000 0.16666667 0.50000000 4.629630e-03

0.50000000 0.16666667 0.66666667 4.629630e-03

0.50000000 0.16666667 0.83333333 4.629630e-03

0.50000000 0.33333333 0.00000000 4.629630e-03

0.50000000 0.33333333 0.16666667 4.629630e-03

0.50000000 0.33333333 0.33333333 4.629630e-03

0.50000000 0.33333333 0.50000000 4.629630e-03

0.50000000 0.33333333 0.66666667 4.629630e-03

0.50000000 0.33333333 0.83333333 4.629630e-03

0.50000000 0.50000000 0.00000000 4.629630e-03

0.50000000 0.50000000 0.16666667 4.629630e-03

0.50000000 0.50000000 0.33333333 4.629630e-03

0.50000000 0.50000000 0.50000000 4.629630e-03

0.50000000 0.50000000 0.66666667 4.629630e-03

0.50000000 0.50000000 0.83333333 4.629630e-03

0.50000000 0.66666667 0.00000000 4.629630e-03

0.50000000 0.66666667 0.16666667 4.629630e-03

0.50000000 0.66666667 0.33333333 4.629630e-03

0.50000000 0.66666667 0.50000000 4.629630e-03

0.50000000 0.66666667 0.66666667 4.629630e-03

0.50000000 0.66666667 0.83333333 4.629630e-03

0.50000000 0.83333333 0.00000000 4.629630e-03

0.50000000 0.83333333 0.16666667 4.629630e-03

0.50000000 0.83333333 0.33333333 4.629630e-03

0.50000000 0.83333333 0.50000000 4.629630e-03

0.50000000 0.83333333 0.66666667 4.629630e-03

0.50000000 0.83333333 0.83333333 4.629630e-03

0.66666667 0.00000000 0.00000000 4.629630e-03

0.66666667 0.00000000 0.16666667 4.629630e-03

0.66666667 0.00000000 0.33333333 4.629630e-03

0.66666667 0.00000000 0.50000000 4.629630e-03

0.66666667 0.00000000 0.66666667 4.629630e-03

0.66666667 0.00000000 0.83333333 4.629630e-03

0.66666667 0.16666667 0.00000000 4.629630e-03

0.66666667 0.16666667 0.16666667 4.629630e-03

0.66666667 0.16666667 0.33333333 4.629630e-03

0.66666667 0.16666667 0.50000000 4.629630e-03

0.66666667 0.16666667 0.66666667 4.629630e-03

0.66666667 0.16666667 0.83333333 4.629630e-03

0.66666667 0.33333333 0.00000000 4.629630e-03

0.66666667 0.33333333 0.16666667 4.629630e-03

0.66666667 0.33333333 0.33333333 4.629630e-03

0.66666667 0.33333333 0.50000000 4.629630e-03

0.66666667 0.33333333 0.66666667 4.629630e-03

0.66666667 0.33333333 0.83333333 4.629630e-03

0.66666667 0.50000000 0.00000000 4.629630e-03

0.66666667 0.50000000 0.16666667 4.629630e-03

0.66666667 0.50000000 0.33333333 4.629630e-03

0.66666667 0.50000000 0.50000000 4.629630e-03

0.66666667 0.50000000 0.66666667 4.629630e-03

0.66666667 0.50000000 0.83333333 4.629630e-03

0.66666667 0.66666667 0.00000000 4.629630e-03

0.66666667 0.66666667 0.16666667 4.629630e-03

0.66666667 0.66666667 0.33333333 4.629630e-03

0.66666667 0.66666667 0.50000000 4.629630e-03

0.66666667 0.66666667 0.66666667 4.629630e-03

0.66666667 0.66666667 0.83333333 4.629630e-03

0.66666667 0.83333333 0.00000000 4.629630e-03

0.66666667 0.83333333 0.16666667 4.629630e-03

0.66666667 0.83333333 0.33333333 4.629630e-03

0.66666667 0.83333333 0.50000000 4.629630e-03

0.66666667 0.83333333 0.66666667 4.629630e-03

0.66666667 0.83333333 0.83333333 4.629630e-03

0.83333333 0.00000000 0.00000000 4.629630e-03

0.83333333 0.00000000 0.16666667 4.629630e-03

0.83333333 0.00000000 0.33333333 4.629630e-03

0.83333333 0.00000000 0.50000000 4.629630e-03

0.83333333 0.00000000 0.66666667 4.629630e-03

0.83333333 0.00000000 0.83333333 4.629630e-03

0.83333333 0.16666667 0.00000000 4.629630e-03

0.83333333 0.16666667 0.16666667 4.629630e-03

0.83333333 0.16666667 0.33333333 4.629630e-03

0.83333333 0.16666667 0.50000000 4.629630e-03

0.83333333 0.16666667 0.66666667 4.629630e-03

0.83333333 0.16666667 0.83333333 4.629630e-03

0.83333333 0.33333333 0.00000000 4.629630e-03

0.83333333 0.33333333 0.16666667 4.629630e-03

0.83333333 0.33333333 0.33333333 4.629630e-03

0.83333333 0.33333333 0.50000000 4.629630e-03

0.83333333 0.33333333 0.66666667 4.629630e-03

0.83333333 0.33333333 0.83333333 4.629630e-03

0.83333333 0.50000000 0.00000000 4.629630e-03

0.83333333 0.50000000 0.16666667 4.629630e-03

0.83333333 0.50000000 0.33333333 4.629630e-03

0.83333333 0.50000000 0.50000000 4.629630e-03

0.83333333 0.50000000 0.66666667 4.629630e-03

0.83333333 0.50000000 0.83333333 4.629630e-03

0.83333333 0.66666667 0.00000000 4.629630e-03

0.83333333 0.66666667 0.16666667 4.629630e-03

0.83333333 0.66666667 0.33333333 4.629630e-03

0.83333333 0.66666667 0.50000000 4.629630e-03

0.83333333 0.66666667 0.66666667 4.629630e-03

0.83333333 0.66666667 0.83333333 4.629630e-03

0.83333333 0.83333333 0.00000000 4.629630e-03

0.83333333 0.83333333 0.16666667 4.629630e-03

0.83333333 0.83333333 0.33333333 4.629630e-03

0.83333333 0.83333333 0.50000000 4.629630e-03

0.83333333 0.83333333 0.66666667 4.629630e-03

0.83333333 0.83333333 0.83333333 4.629630e-03

Phonon calculation

&inputph

prefix = 'ZrB2',

fildyn = 'ZrB2.dyn',

amass(1) = 91.224,

amass(2) = 10.811,

outdir = './'

ldisp = .true.,

trans = .true.,

fildvscf = 'dvscf',

nq1=6,

nq2=6,

nq3=6,

tr2_ph = 1.0d-14

search_sym = .False./

Wannier function calculation

begin projections

Zr:l=0;l=1;l=2

```
B:l=0;l=1
end projections
guiding_centres=.true.
num_bands = 20
num_wann = 17
dis_froz_max = 11.5
dis_win_max = 35
dis_conv_tol = 1.0d-13
dis_mix_ratio = 0.9
dis_num_iter =  20000
num_iter  =   6000
num_print_cycles = 100
begin unit_cell_cart
3.1624766105279010   -0.0000000032701280   -0.0000000000000000
-1.5812378109279781    2.7387850827611713    0.0000000000000000
-0.0000000000000000    0.0000000000000000    3.5311016001481890
end unit_cell_cart
begin atoms_frac
Zr  -0.0000000000000000  0.0000000000000000  0.0000000000000000
B    0.3333330000000032  0.6666669999999968  0.5000000000000000
B    0.6666669999999968  0.3333330000000032  0.5000000000000000
end atoms_frac
write_xyz=.true.
```

write_u_matrices = .true.

bands_plot = true

bands_plot_format = gnuplot

bands_num_points = 100

begin kpoint_path

G 0.0 0.0 0.0 M 0.5 0.0 0.0

M 0.5 0.0 0.0 K 0.33 0.33 0.0

K 0.33 0.33 0.0 G 0.0 0.0 0.0

G 0.0 0.0 0.0 A 0.0 0.0 0.5

A 0.0 0.0 0.5 L 0.5 0.0 0.5

end kpoint_path

mp_grid : 4 4 4

begin kpoints

0.00000000 0.00000000 0.00000000

0.00000000 0.00000000 0.25000000

0.00000000 0.00000000 0.50000000

0.00000000 0.00000000 0.75000000

0.00000000 0.25000000 0.00000000

0.00000000 0.25000000 0.25000000

0.00000000 0.25000000 0.50000000

0.00000000 0.25000000 0.75000000

0.00000000 0.50000000 0.00000000

0.00000000 0.50000000 0.25000000

0.00000000 0.50000000 0.50000000

0.00000000 0.50000000 0.75000000

0.00000000 0.75000000 0.00000000

0.00000000 0.75000000 0.25000000

0.00000000 0.75000000 0.50000000

0.00000000 0.75000000 0.75000000

0.25000000 0.00000000 0.00000000

0.25000000 0.00000000 0.25000000

0.25000000 0.00000000 0.50000000

0.25000000 0.00000000 0.75000000

0.25000000 0.25000000 0.00000000

0.25000000 0.25000000 0.25000000

0.25000000 0.25000000 0.50000000

0.25000000 0.25000000 0.75000000

0.25000000 0.50000000 0.00000000

0.25000000 0.50000000 0.25000000

0.25000000 0.50000000 0.50000000

0.25000000 0.50000000 0.75000000

0.25000000 0.75000000 0.00000000

0.25000000 0.75000000 0.25000000

0.25000000 0.75000000 0.50000000

0.25000000 0.75000000 0.75000000

0.50000000 0.00000000 0.00000000

0.50000000 0.00000000 0.25000000

0.50000000 0.00000000 0.50000000

0.50000000 0.00000000 0.75000000

0.50000000 0.25000000 0.00000000

0.50000000 0.25000000 0.25000000

0.50000000 0.25000000 0.50000000

0.50000000 0.25000000 0.75000000

0.50000000 0.50000000 0.00000000

0.50000000 0.50000000 0.25000000

0.50000000 0.50000000 0.50000000

0.50000000 0.50000000 0.75000000

0.50000000 0.75000000 0.00000000

0.50000000 0.75000000 0.25000000

0.50000000 0.75000000 0.50000000

0.50000000 0.75000000 0.75000000

0.75000000 0.00000000 0.00000000

0.75000000 0.00000000 0.25000000

0.75000000 0.00000000 0.50000000

0.75000000 0.00000000 0.75000000

0.75000000 0.25000000 0.00000000

0.75000000 0.25000000 0.25000000

0.75000000 0.25000000 0.50000000

0.75000000 0.25000000 0.75000000

```
  0.75000000  0.50000000  0.00000000
  0.75000000  0.50000000  0.25000000
  0.75000000  0.50000000  0.50000000
  0.75000000  0.50000000  0.75000000
  0.75000000  0.75000000  0.00000000
  0.75000000  0.75000000  0.25000000
  0.75000000  0.75000000  0.50000000
  0.75000000  0.75000000  0.75000000
end kpoints

&inputpp
  outdir='./tmp/'
  prefix = 'ZrB2'
  seedname = 'ZrB2'
  write_mmn = .true.
  write_amn = .true.
/
```

Resistivity calculation

```
&inputepw
  prefix      = 'ZrB2',
  amass(1)    = 91.224,
  amass(2)    = 10.811
```

```
 outdir      = './'
elph        = .true.
 kmaps       = .false.
 epbwrite    = .true.
 epbread     = .false.
 epwwrite    = .true.
 epwread     = .false.
scattering_serta = .true.
 nbndsub     =  5
 nbndskip    =  0
 wannierize  = .true.
 num_iter    = 300
 dis_win_max = 21
 dis_win_min = -3
 dis_froz_min= -3
 dis_froz_max= 13.5
proj(1)     = 'B:pz'
 proj(2)     = 'f=0.5,1.0,0.5:s'
 proj(3)     = 'f=0.0,0.5,0.5:s'
 proj(4)     = 'f=0.5,0.5,0.5:s'

 wdata(1) = 'bands_plot = .true.'
 wdata(2) = 'begin kpoint_path'
```

```
 wdata(3) = 'G 0.00 0.00 0.00 X 0.00 0.50 0.50'
 wdata(4) = 'X 0.00 0.50 0.50 W 0.25 0.50 0.75'
 wdata(5) = 'W 0.25 0.50 0.75 L 0.50 0.50 0.50'
 wdata(6) = 'L 0.50 0.50 0.50 K 0.375 0.375 0.75'
 wdata(7) = 'K 0.375 0.375 0.75 G 0.00 0.00 0.00'
 wdata(8) = 'G 0.00 0.00 0.00 L 0.50 0.50 0.50'
 wdata(9) = 'end kpoint_path'
 wdata(10) = 'bands_plot_format = gnuplot'
 iverbosity  = 0
 elecselfen  = .true.
 phonselfen  = .false.
efermi_read = .true.
fermi_energy = 15.442

 fsthick     = 2 ! eV
 eptemp      = 0.075 ! K
 degaussw    = 0.05 ! eV
 a2f         = .false.
 dvscf_dir   = '../save'
 nkf1        = 20
 nkf2        = 20
 nkf3        = 20
 nqf1        = 20
```

nqf2 = 20

nqf3 = 20

nk1 = 6

nk2 = 6

nk3 = 6

nq1 = 6

nq2 = 6

nq3 = 6

/

28 cartesian

0.000000000000000E+00 0.000000000000000E+00 0.000000000000000E+00

0.000000000000000E+00 0.000000000000000E+00 0.149078254326549E+00

0.000000000000000E+00 0.000000000000000E+00 0.298156508653098E+00

0.000000000000000E+00 0.000000000000000E+00 -0.447234762979648E+00

0.000000000000000E+00 0.192450089729846E+00 0.000000000000000E+00

0.000000000000000E+00 0.192450089729846E+00 0.149078254326549E+00

0.000000000000000E+00 0.192450089729846E+00 0.298156508653098E+00

0.000000000000000E+00 0.192450089729846E+00 -0.447234762979648E+00

0.000000000000000E+00 0.384900179459692E+00 0.000000000000000E+00

0.000000000000000E+00 0.384900179459692E+00 0.149078254326549E+00

0.000000000000000E+00 0.384900179459692E+00 0.298156508653098E+00

0.000000000000000E+00 0.384900179459692E+00 -0.447234762979648E+00

0.000000000000000E+00 -0.577350269189538E+00 0.000000000000000E+00

0.000000000000000E+00 -0.577350269189538E+00 0.149078254326549E+00

0.000000000000000E+00 -0.577350269189538E+00 0.298156508653098E+00

0.000000000000000E+00 -0.577350269189538E+00 -0.447234762979648E+00

0.166666666666653E+00 0.288675134594769E+00 0.000000000000000E+00

0.166666666666653E+00 0.288675134594769E+00 0.149078254326549E+00

0.166666666666653E+00 0.288675134594769E+00 0.298156508653098E+00

0.166666666666653E+00 0.288675134594769E+00 -0.447234762979648E+00

0.166666666666653E+00 0.481125224324615E+00 0.000000000000000E+00

0.166666666666653E+00 0.481125224324615E+00 0.149078254326549E+00

0.166666666666653E+00 0.481125224324615E+00 0.298156508653098E+00

0.166666666666653E+00 0.481125224324615E+00 -0.447234762979648E+00

0.333333333333306E+00 0.577350269189538E+00 0.000000000000000E+00

0.333333333333306E+00 0.577350269189538E+00 0.149078254326549E+00

0.333333333333306E+00 0.577350269189538E+00 0.298156508653098E+00

0.333333333333306E+00 0.577350269189538E+00 -0.447234762979648E+00

Scattering rate calculation

&perturbo

prefix = 'ZrB2'

calc_mode = 'imsigma'

fklist = 'ZrB2_tet.kpt'

ftemper = 'ZrB2.temper'

band_min = 10

```
 band_max = 11
 phfreq_cutoff = 0.6 ! meV
 delta_smear = 5 ! meV
 sampling = 'uniform'
 nsamples = 100
/
```